



## Various defects in graphene: a review

 Cite this: *RSC Adv.*, 2022, **12**, 21520

 Mahesh Datt Bhatt, <sup>a</sup> Heeju Kim<sup>ab</sup> and Gunn Kim \*<sup>ab</sup>

 Received 4th March 2022  
 Accepted 19th July 2022

DOI: 10.1039/d2ra01436j

[rsc.li/rsc-advances](https://rsc.li/rsc-advances)

Pristine graphene has been considered one of the most promising materials because of its excellent physical and chemical properties. However, various defects in graphene produced during synthesis or fabrication hinder its performance for applications such as electronic devices, transparent electrodes, and spintronic devices. Due to its intrinsic bandgap and nonmagnetic nature, it cannot be used in nanoelectronics or spintronics. Intrinsic and extrinsic defects are ultimately introduced to tailor electronic and magnetic properties and take advantage of their hidden potential. This article emphasizes the current advancement of intrinsic and extrinsic defects in graphene for potential applications. We also discuss the limitations and outlook for such defects in graphene.

### 1. Introduction

Carbon is essential for life on Earth. It is also important in various technical applications, from pharmaceuticals to synthetic materials. The carbon atom tends to create extensive networks of covalent connections with other elements as well as with itself. It features many different orbital hybridizations. Elemental carbon exists in two natural allotropes: (i) diamond containing  $sp^3$ -hybridized carbon atoms and (ii) graphite containing  $sp^2$ -hybridized carbon atoms. However, in the late 20th and early 21st centuries, fullerenes,<sup>1</sup> carbon nanotubes,<sup>2</sup> and graphene<sup>3</sup> were discovered one after another.

Wallace first investigated single-layer graphene in 1947 theoretically.<sup>4</sup> However, it was first isolated and identified in 2004,<sup>3</sup> though they credit Hans-Peter Boehm and his co-workers for the experimental discovery of graphene in 1962.<sup>5,6</sup> Each carbon atom in graphene bonds three nearest-neighbor carbon atoms with  $sp^2$  hybridization of  $2s$ ,  $2p_x$ , and  $2p_y$  orbitals, and  $2p_z$  orbital forms a delocalized  $\pi$  and  $\pi^*$  bands perpendicular to the graphene plane. The  $\pi$  and  $\pi^*$  bands cross the Dirac point. Graphene has attractive physical properties since the two bands have an almost linear dispersion near the Dirac point. As a result, a vast number of experimental and theoretical research have focused on the applications of graphene in sensors,<sup>7–9</sup> nano-electronic devices,<sup>10,11</sup> spin devices,<sup>12</sup> catalysis,<sup>13</sup> and energy storage.<sup>14–16</sup>

The edge shapes of graphene nanoribbons (GNRs) are very diverse, but the most representative ones are armchairs and zigzag edges.<sup>17,18</sup> The edge geometry is a key parameter that determines the electronic properties of GNRs.<sup>19–22</sup> One of the exciting properties of graphene is its intrinsic magnetism related to  $p$  electrons, which is advantageous over  $d$ - or  $f$ -

electron-based magnetism because of weak spin–orbit interaction and long electron spin coherence time. Although the pristine two-dimensional (2D) infinite graphene is non-magnetic, theories predict and experiments confirm the magnetic moments of zigzag-edged GNRs.<sup>22–25</sup> In this way, pristine graphene shows excellent electronic and magnetic properties at room temperature. However, its zero-band gap does not support the switching operation of graphene-based transistors with a sufficiently high on-off ratio. Therefore, pristine graphene should be modified with some defects for its applications in various electronic devices.<sup>26</sup> Defects in three-dimensional (3D) bulk crystals have been extensively studied for a long time; however, defects in 2D materials were not considered until 2004, when single-layer graphene was first isolated using mechanical exfoliation.<sup>3</sup> The defects in 2D materials were fabricated using different experimental techniques such as chemical vapor deposition (CVD), epitaxial growth, particle irradiation, and chemical functionalization. Dopants change the local electronic structure by injecting charge into the carbon materials. The weaker bond around the defect affects thermal conductivity and mechanical strength. Since carbon atoms have several types of orbital hybridization, stable graphene structures with various defects can be created. Various functionalizations can be used to make GNRs ferromagnetic, antiferromagnetic semimetals, metals, or semiconductors with a wide bandgap.<sup>27–30</sup> Understanding the physical properties of defects in graphene is a vital goal of applied physics.

Creating carbon vacancies or chemical doping can alter the uniform charge distribution of graphene surfaces and improve the stability of supported metals,<sup>26,31–34</sup> resulting in modifying the electronic structure and magnetic properties of graphene systems. If the number of missing atoms is even, the carbon atoms could be fully reconstructed, leaving no dangling bonds. However, if odd numbers of atoms are missing, dangling bonds render the graphene more unstable and reactive. A single metal

<sup>a</sup>Hybrid Materials Center, Sejong University, Seoul 05006, Korea. E-mail: gunnkim@sejong.ac.kr

<sup>b</sup>Department of Physics and Astronomy, Sejong University, Seoul 05006, Korea



(Al, Cu, Au, and Pt) atom bonded to the monovacancy in graphene nanosheets act as highly active catalysts for carbon monoxide (CO) oxidation according to computational simulations.<sup>35–42</sup> For example, some theoretical studies investigated the formation configurations and catalytic properties of more than one heteroatom co-doped graphene sheet for oxygen reduction reactions.<sup>43–46</sup> However, in experiments, atom-scale control of the monovacancy formation is quite tricky, and the natural graphene may contain impurities in preparation processes. Single vacancy defects in graphene have grown much attention.<sup>47–55</sup> Moreover, ring defects and vacancy complexes are also of interest.<sup>56–66</sup> One-dimensional (1D) arrays of topological ring defects have been explored theoretically,<sup>67,68</sup> and ring defect arrays have been imaged experimentally.<sup>69</sup> Experiments and theory have intensely studied the effects of single vacancy defects on graphene's mechanical, electrical, and magnetic properties.<sup>70</sup> Some computational studies predicted that the vacancy defects would reduce Young's modulus of graphene.<sup>54,55,66,71</sup> However, experiments showed that dilute concentrations of single vacancies could harden graphene.<sup>72,73</sup> Large concentrations of single vacancies are expected to weaken graphene. In addition, single vacancies induce the local spin magnetic moment owing to the dangling bond of a single vacancy.<sup>48,54,74</sup> Although the topological 555–777 defect<sup>75</sup> was more stable than separate two monovacancies, there is a lack of investigation into non-metal atom modified divacancy (555–777) structured graphene sheet. Li *et al.*<sup>76</sup> investigated the cooperative interaction of Fe impurity atom bonded to three nitrogen substitutional defects (FeN<sub>3</sub>) aided for the adsorption of CO molecules. They found that the Fe atom is a low-cost, environmentally benign, readily available, and highly efficient catalyst.<sup>42–46,76–80</sup> Previous studies reported the catalytic activity of single-atom Fe-supported graphene,<sup>81</sup> the divacancy in graphene,<sup>82</sup> and graphene oxide.<sup>79</sup> More detailed investigations into ground-state and excited-state electronic structures with single and double vacancies in graphene have been done using density functional theory (DFT).<sup>83–87</sup>

It is well known that atomic defects induce magnetism<sup>88–92</sup> and change local structural configurations.<sup>91,92</sup> Metal atom intercalation beneath graphene<sup>93–95</sup> improves molecular adsorption.<sup>96</sup> The molecular assembly on the surface<sup>97,98</sup> also modifies the electronic properties of graphene.<sup>99,100</sup> Hu *et al.*<sup>95</sup> investigated both in-plane and off-plane defects in epitaxial graphene on the SiC substrate by doping Bi atoms during the graphene growth process. Theoretical studies reported the defect penetration process of Li, H, Si, and Cu atoms through different defects in epitaxial graphene on SiC (0001).<sup>101–104</sup>

Recently, the extended line defect in graphene has been observed.<sup>69,105,106</sup> The extended line defects divide graphene into domains with different orientations and thus affect the electronic, thermal, and magnetic properties of graphene sheets. It has been theoretically reported that the electronic transport behaviors of graphene sheets and GNRs vary remarkably with embedded line defects, and they act as a filter to produce a valley-polarized beam of electrons or holes.<sup>26,28,107–110</sup> Kou *et al.*<sup>109</sup> demonstrated a weak ferromagnetic ground state with spin-polarized electrons localized along the extended line

defects embedded in graphene. They found that the magnetic moment of graphene with the line defects can be tuned by applying in-plane strain.

In this review, we present various studies of structural defects in graphene for their use in potential applications. In the second section, we introduce many types of defects in graphene. Finally, we discuss the key challenges and outlook for the advancements of structural defects in graphene. Although many review articles on different aspects of graphene, such as synthesis, properties, and applications, are published, there is an opportunity to review the latest advancement of structural defects in graphene for their use in potential applications using both experimental and theoretical approaches. In this sense, this review is expected to understand the role of structural defects in graphene and consequently help investigate graphene defects for potential applications.

## 2. Defects in graphene

Several experimental studies have demonstrated native or physically introduced defects in graphene using transmission electron microscopy (TEM)<sup>111–115</sup> and scanning tunneling microscopy.<sup>116</sup> Graphene has two types of defects: (i) natural defects known as intrinsic defects in graphene, such as Stone–Wales defects, single-vacancy defects, multiple-vacancy defects, line defects, and carbon adatoms; and (ii) physically introduced defects known as extrinsic defects in graphene, which are foreign adatoms and substitutional impurities. Point defects such as vacancies or interstitial atoms are typically zero-dimensional (0D). The concept of dislocations is based on one-dimensional (1D) line defects. Grain boundaries or stacking faults are 2D defects. Inclusions and voids are 3D defects. Each defect in graphene has specific mobility, generally governed by an activation barrier that depends on the type of defect and thus increases exponentially with temperature.

### 2.1 Stone–Wales defects

A Stone–Wales (SW) defect is a crystallographic defect that occurs when the connectivity of two-bonded carbon atoms changes, causing them to rotate by 90° relative to the midpoint of their bond (Fig. 1).<sup>26,64,114,117</sup> For the SW (5775) defect, two pentagons, and two heptagons are generated from four hexagons in graphene or carbon nanotubes after rotation of one of the C–C bonds by 90° with a formation energy of about 5 eV and an activation energy barrier of about 10 eV using DFT methods (Fig. 1c).<sup>63,64</sup> The SW structure has a high restoration barrier of about 7 eV.<sup>64,117–123</sup> As a result, it is challenging to restore to its perfect hexagonal network structure, even at high temperatures, once the SW defect is formed, indicating that the formation of the SW defects is a termination step for graphene growth. Rapid cooling from high temperatures or electron beam irradiation can cause SW defects.<sup>26,58</sup> Wang *et al.*<sup>124</sup> proposed that adsorption of the carbon adatom could be used as an effective catalyst for the SW-healing in the post-treatment of graphene by reducing the restoration barrier to a lower value of about 0.86 eV. Openov *et al.*<sup>118</sup> reported wavy sine and cosine-like



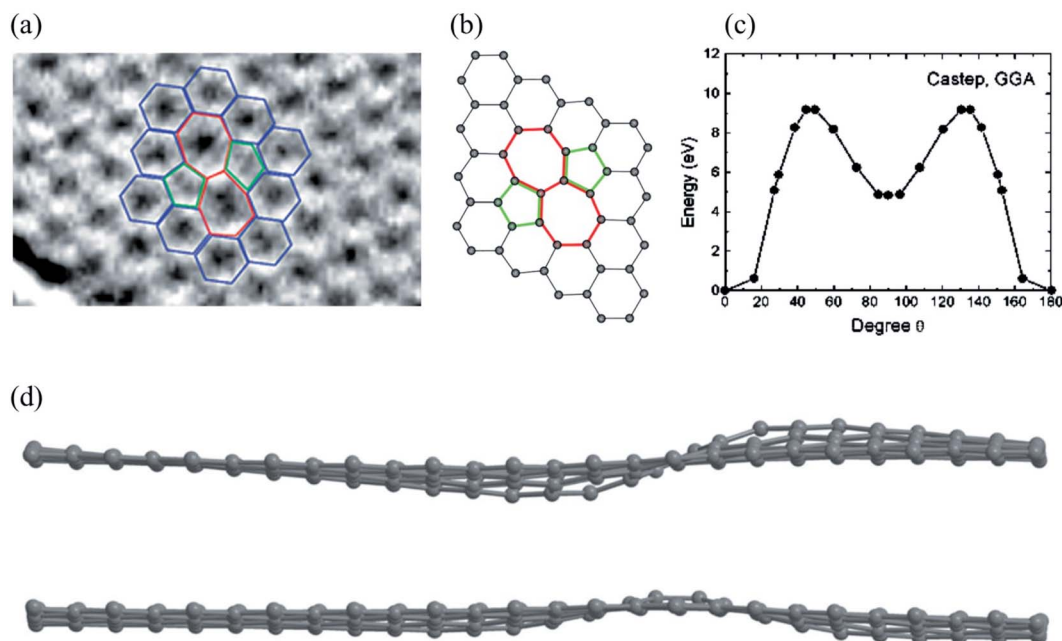


**Fig. 1** Stone–Wales defect SW (5775): (a) experimental TEM image. Reprinted from ref. 113. Copyright 2008 American Chemical Society; (b) DFT calculated image. Reprinted from ref. 26. Copyright 2010 American Chemical Society; (c) DFT calculated energy barrier for bond rotation. Reprinted from ref. 64. Copyright 2005 American Chemical Society; (d) DFT calculated image of sine and cosine like configurations. Reprinted from ref. 118. Copyright 2015 Pleiades Publishing Ltd.

distortions of SW defects in graphene of the amplitude of 1 (Fig. 1d). The SW defects behave as preferential adsorption centers for hydrogen and other chemical elements,<sup>125,126</sup> which is important for several applications.

The SW defect has a calculated penetration barrier below 1 eV and an  $H^+$ -over- $D^+$  selectivity of 7 at room temperature, while hydrogenation also reduces the penetration barrier with significantly lower isotope selectivity.<sup>127</sup> A carbon vacancy and the SW defect play significant roles in the observed p-type behavior, changes in electrical or optoelectronic characteristics, and degradation of graphene under ambient gases ( $N_2$ ,  $O_2$ , Ar, and  $CO_2$ ) or atmospheric oxygen.<sup>128</sup> The single vacancy and SW defects could decrease the current through the graphene nanodevices using the ballistic transport model, accompanied by defect-induced electron transmission peaks,<sup>129</sup> signifying that this method can hopefully be used to study the influence of multiple vacancy chains on the electronic transport properties of graphene nanodevices.<sup>130</sup> For the zigzag-direction loading, slip nucleates in the SW defect through the formation of two pentagons and a twisted hexagon. In contrast, for the armchair-direction loading, healing, generation, and pentagon–heptagon pair separation of the SW defect occur *via*  $90^\circ$  rotation of the C–C bond.<sup>131</sup> There are two distinct orientations of the SW defects, namely, types I and II, caused by the  $90^\circ$  rotation of the C–C bond in different directions. Ebrahimi *et al.*<sup>132</sup> studied the effects of the orientations and concentrations of the SW defects on the thermal conductivity of zigzag and armchair GNRs using the reverse nonequilibrium molecular dynamics method. It is found that the thermal conductivity of GNRs with two different chirality cases reaches its minimum in the range of 0.1–0.7%

defect concentration, with more significant thermal conductivity of zigzag GNRs with type II defects than the GNRs with type I defects at high concentrations of the SW defects.

The SW defect in graphene is expected to modify its vibration and be seen in its Raman spectrum. The introduction of SW defects in graphene is also expected to affect the mechanical properties of graphene. Molecular dynamics (MD) simulations predicted that SW defects dramatically reduce the strain failure and the intrinsic strength of the monolayer graphene sheet. The SW defects in graphene can modify its physical properties and change its chemical properties by acting as active sites for the adsorption of other atoms and molecules and increasing the local chemical reactivity. DFT calculations predicted that SW defects in graphene strongly influence hydrogen chemical reactivity.<sup>133</sup> Similarly, SW defects in graphene can enhance the adsorption of Li, Na, K, and Ca atoms because of better electron transfer between the adatom and the defective graphene sheet. Therefore, SW defects in graphene are much more suitable for its use in transistors, hydrogen storage, and high-capacity anode material in metal (Li, Na, K, and Ca)-ion batteries.<sup>62,134–138</sup>

## 2.2 Single vacancy defects

A single vacancy (SV) in graphene is generated by missing a single carbon atom. Previous experimental and theoretical studies have observed single vacancies (SV) in graphene using TEM<sup>112,113</sup> and STM.<sup>49,139,140</sup> Fig. 2 shows a TEM image of the single vacancy defect and the corresponding atomic model.<sup>26,114</sup> Because of the Jahn–Teller distortion, two of three dangling bonds are saturated and pointed towards the missing atom. One of them always remains because of geometrical reasons.



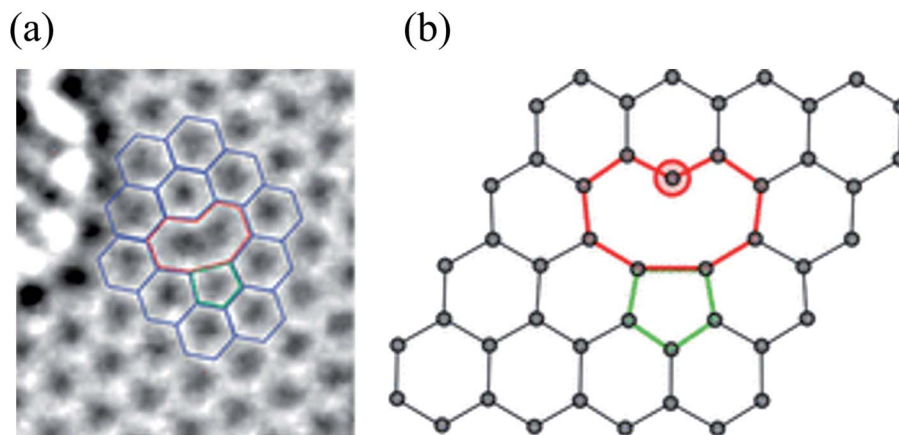


Fig. 2 Single vacancy defect in graphene: (a) experimental TEM image. Reprinted with permission from ref. 113. Copyright 2008 American Chemical Society and (b) atomic structure as obtained from DFT calculations. Reprinted with permission from ref. 26. Copyright 2010 American Chemical Society.

The monovacancy with such a dangling bond requires higher formation energy of 7.5 eV than the Stone–Wales defect, and the corresponding migration barrier is  $\sim 1.3$  eV at 100–200 °C.<sup>84,141</sup> Many theoretical studies have been devoted to the diffusion of vacancies and the structural changes produced in graphene.<sup>49,85,142</sup> The magnetic moment arising from an SV is attributed to the presence of unpaired electrons created by removing a carbon atom.<sup>85</sup> DFT calculations for an SV showed that the presence of the vacancy produces a pentagon-like structure because of the formation of a weak covalent bond between two atoms surrounding the vacancy. Among the three dangling bonds, the third bond plays a vital role in creating the magnetic moment of about  $1.04 \mu_B$  in pure nonmagnetic graphene.<sup>85</sup> The experimentally determined magnetic moments of graphene with vacancies and traces of room temperature ferromagnetism are still disputatious and debatable.<sup>143–146</sup> Valencia *et al.*<sup>147</sup> predicted a magnetic moment of  $2 \mu_B$  for the SV in graphene. They found that periodic arrays of single vacancies may provide interesting spin–spin interactions because of the specific symmetry of the graphene lattice. Kim *et al.*<sup>148</sup> studied the effect of vacancies and tensile strain on the quality factor for mass sensing using graphene monolayers with an SV at the center. Therefore, the effect of multiple SVs and their randomly distributed positions on graphene nanosheets' performance needs more consideration. Graphene sheets in zigzag and armchair directions exhibit slightly different Young's moduli ranging from 1.20 to 1.10 TPa in the zigzag direction and from 1.12 to 1.09 TPa in the armchair direction using continuum modeling.<sup>149</sup> Repeating vacancy or divacancies in GNR induce metallization and magnetization in nonmagnetic semiconducting nanoribbons because of the spin polarization of local defect states. The antiferromagnetic ground state of semiconducting zigzag ribbons can change to a ferrimagnetic state upon creating vacancy defects.<sup>113</sup> Defects significantly influence the mechanical properties of graphene. Wang *et al.*<sup>150</sup> investigated the mechanical behaviors of defective graphene sheets with vacancies using MD simulations. They found that

vacancies cause a considerable loss of strength, and the fracture strength is sensitive to the loading directions and temperature.

Carpenter *et al.*<sup>151,152</sup> reported the vacancy-induced amorphization and the mechanical properties of irradiated single-layer graphene using MD simulations. They found a critical range of vacancy concentrations, leading to a qualitative change in the fracture response from brittle to ductile. The fracture strength of graphene is lost by about 17.7% because of a single vacancy. Despite the recent progress, little is known about the evolution of defective graphene morphology during tension.<sup>153</sup> SV and SW defects can be created when rapid quenching occurs or when the graphene is irradiated. Some researchers have extensively investigated these defects.<sup>65,154,155</sup> A recent study has determined that the activation energy for the diffusion of a single vacancy in graphene is extremely sensitive to in-plane uniaxial strain, both parallel and perpendicular to the direction of the hopping motion of a single vacancy, with the barrier doubled or halved with a respective tensile or compressive strain of just 2–3%.<sup>55,156</sup> in applications of investigating the elastic properties of graphene.

### 2.3 Multiple vacancy defects

Double vacancy (DV) means either coalescence of two single vacancies (SVs) or removal of two neighboring carbon atoms. DV can be reconstructed, resulting in two pentagons and one octagon labeled the 5–8–5 defect. Fig. 3 shows the atomic structures of divacancies obtained by DFT and experimental TEM images.<sup>157</sup> Previous studies reported the formation energy of about 8 eV for DV, which is 4 eV per atom, comparatively less than that of an SV.<sup>84,141</sup> It means that the DV is energetically more stable than the SV. In the presence of dangling bonds, the material becomes very unstable and tends to chemically bond with impurity atoms or molecules. The SV defect causes a dangling bond, whereas the 5–8–5 defect causes only local deformation. As a saturated eight-membered ring compound, a cyclooctane molecule,  $(\text{CH}_2)_8$ , also has a non-planar structure that looks like a crown or a boat. Since the 5–8–5 defect also has



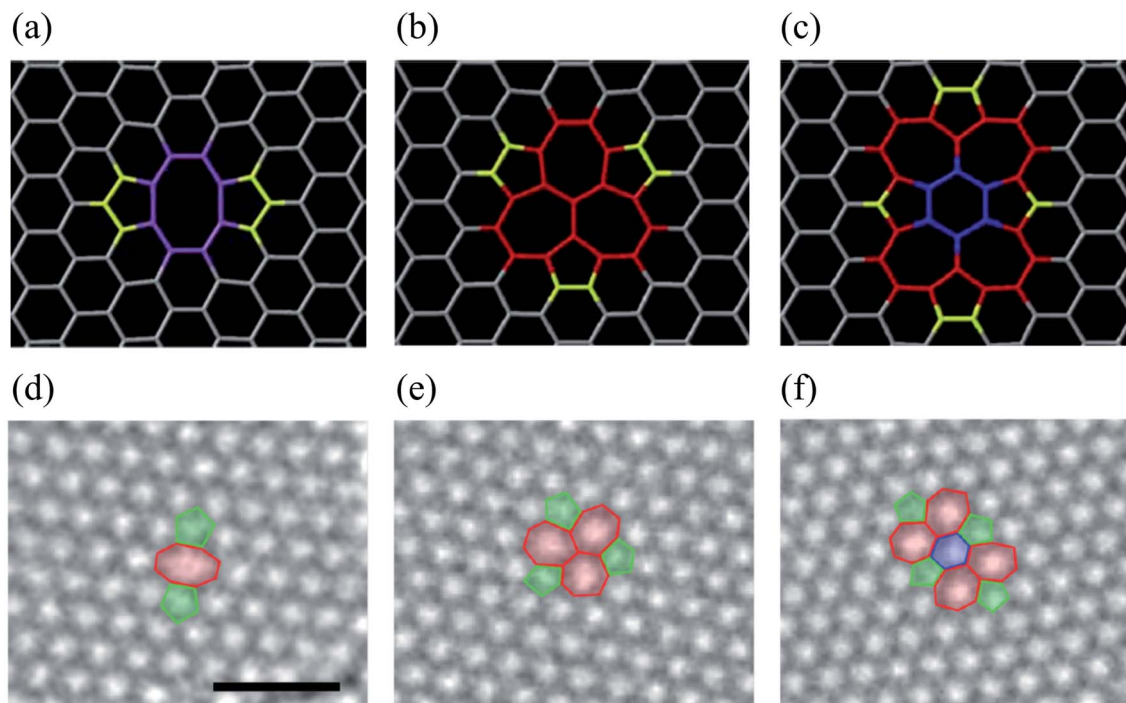


Fig. 3 DV defects in graphene. (a–c) Atomic structures obtained from DFT calculations. Reprinted with permission from ref. 157. Copyright 2016 IOP Publishing. (d–f) Experimental TEM images corresponding to the atomic models in (a–c), respectively. Reprinted with permission from ref. 26. Copyright 2008 American Chemical Society. Here, (a and d) the 5–8–5 defect, (b and e) the 555–777 defect, and (c and f) the 5555–6–7777 defect.

a considerable local curvature, the system is changed to the 555–777 or 5555–6–7777 defect to reduce the local curvature. Therefore, all three defect structures can be found when observed with TEM, as shown in Fig. 3. The defect transformation will be described in detail later.

Removing more than two carbon atoms, known as multiple vacancy defects, may lead to larger and more complex defect configurations. In this regard, one would expect to observe a more-or-less random set of vacancies. Therefore, it seems possible for the lattice to reconstruct locally around the vacancies and form a random set of non-hexagonal polygons. Two pentagons and one octagon appear for a fully reconstructed double vacancy, leading to no dangling bond. A collaborative experimental and theoretical study of graphene divacancy revealed a non-hexagonal rearranged flat structure with no magnetic traces.<sup>158</sup> The divacancy (DV) and larger vacancies could be frequently created by the current physical and chemical treatment, even though the SV has been more widely studied.<sup>50,159–162</sup> TEM results indicate that multiple vacancies, rather than monovacancies, are produced more easily under electron irradiation conditions.<sup>111</sup> Theoretical calculations at different levels of theory also point out that the formation energies of the DV in carbon nanotubes and graphene are much lower than monovacancy (SV) formation energies.<sup>57,87,141,163,164</sup> The presence of more than one vacancy and their mutual relationship significantly alters the magnetization phenomenon in graphene because of the creation of sublattice imbalance.<sup>75,165,166</sup> Wang *et al.*<sup>130</sup> systematically investigated the

electronic transport properties of various defects in graphene, such as SW defect, SV, DV, and multiple vacancy chains using first-principles calculations combined with the non-equilibrium Green's function method. They found that some defect-induced electronic states can enormously enhance the transport of electrons between electrodes at certain energy levels. In contrast, others are only localized around the defect sites and could be identified using a small source-drain voltage and sweeping the gate voltage applied to the graphene field-effect transistors.

Lee *et al.*<sup>57</sup> reported the spontaneous reconstruction and transformation of the 5–8–5 defect into a more stable form of the 555–777 defect consisting of three pentagon/heptagon pairs. Kim *et al.*<sup>75</sup> also studied the same transformation and reported that the activation energy barrier of the change of 5–8–5 into 555–777 defect was around 5.3 eV. Cretu *et al.*<sup>167</sup> showed that the formation energy of the 5555–6–7777 defect (formed by a bond rotation from the 555–777 of 30° for the graphene sheet and consisting of four pentagons and four heptagons recently observed in a few TEM experiments<sup>58,168</sup>) lies in between that of forms 5–8–5 and 555–777. The rotation barrier is around 6 eV. All these migration steps are undoubtedly interesting in understanding the behavior of defects in graphene, but the picture is still probably quite incomplete.

Recent studies have revealed that multiple vacancies in graphene can create substantial and inhomogeneous displacement strain that extends far into the surrounding lattice. This is caused by the reconstruction induced by the pair-wise removal



of dangling bonds.<sup>66,108,169–171</sup> Moreover, in a regular arrangement, multiple divacancies can form chain-like line defects, known as extended line defects (ELDs). Four types of extended line defects (5–8–5, 55–77, and 555–777 defects for armchair GNRs, 48 defects for zigzag GNRs) were mainly observed in experiments,<sup>58,172</sup> and the formation of chain structure could be controlled precisely.<sup>69</sup> The influence of the 5–8–5, 55–77, and 555–777 ELDs on the thermal transport properties of the armchair graphene nanoribbon was also reported.<sup>173</sup>

## 2.4 Carbon adatom defects

When a carbon adatom is adsorbed on a defect-free graphene sheet, forming two covalent C–C bonds between the adatom and the underlying carbon atoms in the graphene sheet, the adsorption energy of the C adatom is about 1.5–2.0 eV with the migration barrier of  $\sim 0.4$  eV.<sup>174,175</sup> The adsorption position of the C adatom is a bridge site between two carbon atoms in the graphene sheet.<sup>176</sup> Since the triangular structure caused by the adsorbed carbon atom is unstable, the adsorbed atom moves quickly on the graphene surface with a high-speed migration rate. Therefore, it is challenging to capture the C adatoms using microscopic techniques such as TEM, STM, *etc.* There is no relevant research on the experimental observation of carbon adatoms on the graphene surface. However, based on the earlier studies on the activation mechanism of activated carbon, carbon and oxygen atoms can migrate on the surface of the carbon layer. Therefore, the existence of out-of-plane carbon adatoms can be confirmed. On the other hand, carbon adatoms are generated under electron irradiation in aberration-correlated transmitted electron microscopy (AC-TEM) or as contaminants in the growth of graphene.<sup>111,177,178</sup> The adatoms are viewed to form a bridge-like structure on the graphene surface under TEM,<sup>111</sup> and bridging atoms can be found in reconstructions of vacancies (odd vacancies).<sup>177</sup> Such adatoms can catalyze the formation and dissociation of bonds in graphene because of their undercoordination for bulk  $sp^2$  carbon atoms. Still, their precise role and observation in common compound defects in graphene remain unclear.<sup>179</sup> Ataca *et al.*<sup>180</sup> investigated the adsorption of carbon adatoms on graphene and its nanoribbons using DFT methods. They found that carbon adatoms prefer to adsorb to the bridge sites and modify graphene's electronic and magnetic properties. The adsorption site geometry with carbon adatom and charge density contour plots in the lateral plane and a vertical plane (perpendicular to the  $x$ -axis) are shown in Fig. 4a–d. Band structures and corresponding density of states calculated for a  $2 \times 2$  supercell are demonstrated in Fig. 4e. The binding energy was the maximum at the bridge site (Fig. 4a). The top site adsorption was observed with a local minimum of 0.3 eV higher energy (Fig. 4b). The C–C bond elongated below  $C'$ , and its charge was slightly delocalized (Fig. 4c and d). The charge density analysis indicated that the orbitals of  $C'$  are combined with  $\pi$  and  $\pi^*$  orbitals of bare graphene, forming new bands near the Fermi level (Fig. 4e). The flat band driven from perpendicular  $sp^2$  orbitals was filled and gave rise to a peak at an energy of  $\sim 2$  eV below the Fermi level in the total density of states. Bands generated from hybridizing

other  $sp^2$  orbitals of  $C'$  with the  $\pi$  and  $\pi^*$  states of graphene occurred near the Fermi level and attributed a metallic character. The band above the Fermi level was generated because of an antibonding combination of p-orbital of  $C'$  perpendicular to the C–C–C plane and  $\pi^*$  states of graphene. Wang *et al.*<sup>124</sup> investigated the adsorption of carbon adatoms in graphene *via* a mechanically different process. They found a relatively tiny restoration barrier of about 0.87 eV using DFT methods, which could make the SW-healing experimentally accessible. Subsequently, the C-adatom can migrate very quickly on the graphene surface. They claimed that their proposed carbon-adatom catalytic mechanism played a crucial role in healing the SW defect during the growth of graphene.

Zhang *et al.*<sup>157</sup> reported that a developed three-center tight-binding model for carbon<sup>181</sup> exhibits excellent band structures, binding energies, and other properties of various carbon crystalline structures and surfaces in excellent agreement with first-principles calculations and experimental results available in the literature. They also searched for the stable forms of vacancies and embedded atoms of various sizes and made systematic calculations to understand better the stable structures and energies of various vacancy and embedded-atom defects in graphene. Consequently, the structural change during the initial stages of activation will help tune the processing of such out-of-plane carbon adatoms to different applications for molecular sieving,<sup>182</sup> gas storage,<sup>183</sup> catalysis,<sup>184</sup> hydrogen storage,<sup>185</sup> and lithium-ion batteries.<sup>186</sup>

## 2.5 Foreign adatom defects

During the process, metal atoms or oxygen-containing functional groups are incorporated into the surface of graphene during the CVD or by a strong oxidation method. The effect of a foreign (noncarbon) adatom on graphene properties depends on the bonding between the adatom and graphene. Such impurity atoms on the graphene layer are bonded with the nearest carbon atoms with covalent bonding or weak van der Waals interaction.<sup>187</sup> Dispersive forces increase the adsorption strength by 0.35 eV. Because the bond between foreign impurity atoms and graphene is weak, the impurity atoms can move on the graphene surface.<sup>167,188,189</sup> However, few experimental studies have reported the migration of foreign impurity atoms.

Low migration barriers in the range of 0.2–0.8 eV have been found in theoretical investigations, implying high adatom mobility at room temperature.<sup>190</sup> Many researchers have performed DFT calculations of the adsorption of various metal atoms<sup>191–205</sup> to investigate energetically stable adsorption sites and their effects on graphene's structural, electronic, and magnetic properties. When Au atoms are bonded to graphene, electrons are transferred from graphene to Au atoms, making the graphene p-doped. When the other transition metal (TM) atoms are attached to graphene, electrons are transferred from the TM atoms to the graphene, and the graphene becomes n-doped. Early TM atoms show significant magnetism to graphene since fewer than five electrons are filled in the d shell. In contrast, the local magnetic moments of late TM atoms with more than five electrons in the d shell decrease.<sup>206</sup> The work



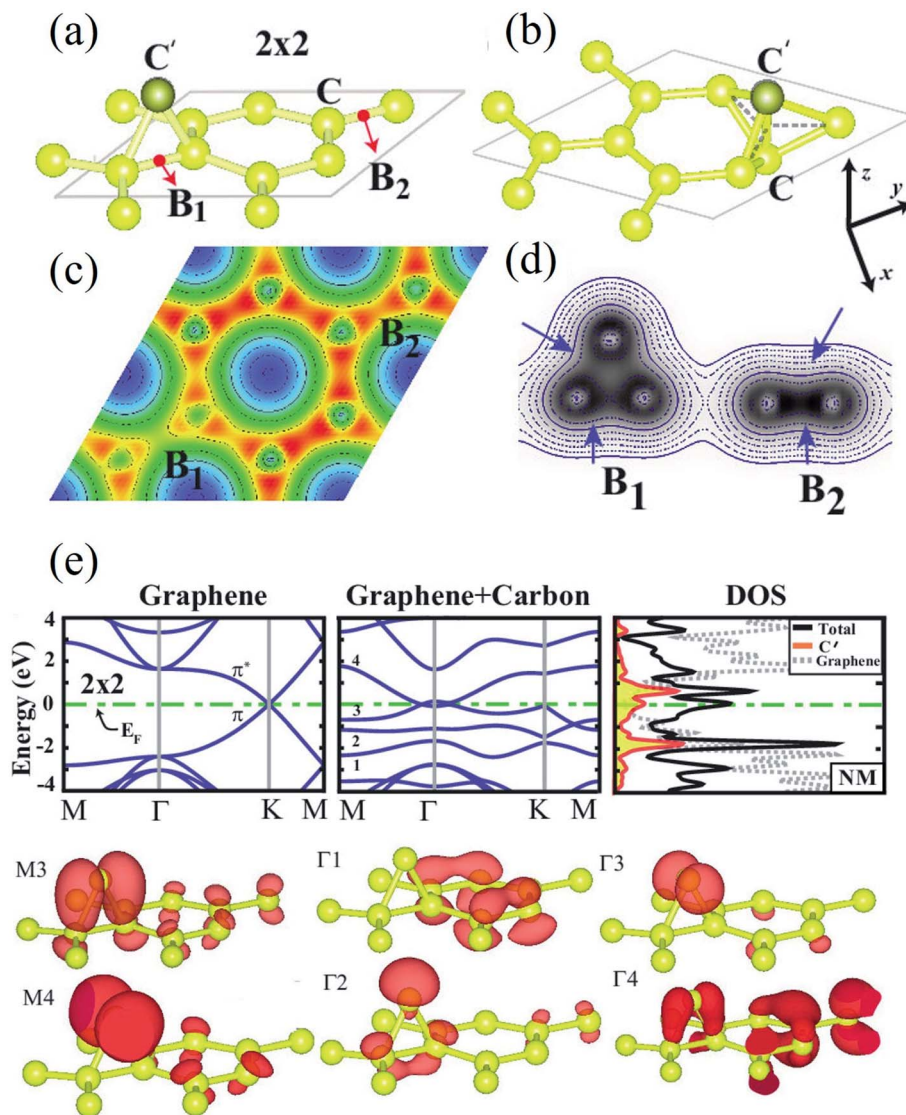


Fig. 4 (a) The bridge site bonding geometry of carbon adatom  $C'$ ; (b) adsorption geometry of carbon adatom  $C'$  at the top site; and (c) charge density contour plots in the  $(x, y)$  plane as well as (d) in a vertical plane (perpendicular to the  $x$ -axis) for bridge site bonding. (e) Band structures and corresponding density of states calculated for a  $2 \times 2$  supercell. Reprinted with permission from ref. 180. Copyright 2011 American Institute of Physics.

function of metal-doped graphene falls with increasing metal adatom concentration and becomes saturated at specified values. The saturation values of the work function for Cs-, Rb-, K-, Na-, and Li-doped graphene sheets were 2.05, 2.18, 3.24, 2.42, and 2.49 eV, respectively. When electrons move from the metal dopant to the clean graphene, the graphene becomes n-doped, and the Fermi energy rises above the Dirac point for all metal atoms investigated. Then, the work function is significantly reduced.<sup>207,208</sup>

Recent experimental studies on graphene have focused on the interaction of transition metals with graphene on the atomic scale, and various experimental tools have been utilized.<sup>188,209–214</sup> One of the important tools to probe the resonant effects between graphene and metal nanoparticles (NPs) is surface-enhanced Raman spectroscopy (SERS). Significant

Raman enhancements for various laser excitations have been reported due to near-field plasmonic effects near metal NPs and graphene.<sup>215,216</sup> Ulrich *et al.*<sup>209</sup> studied the enhanced electron-phonon interaction by monitoring the surface plasmon resonance effect in the Ag-graphene hybrid structure. Park *et al.*<sup>217</sup> investigated the Au NPs-graphene-Au film junction (hybrid system) to identify the layer breathing mode and other out-of-plane phonon modes of few-layer graphene through SERS. Zandiatashbar *et al.*<sup>72</sup> utilized a modified oxygen plasma technique to incorporate defects in pristine graphene in a controlled fashion. They also used Raman spectroscopy and transmission electron microscopy to characterize the defects, then used AFM nano-indentation to quantify the stiffness and strength of defective graphene experimentally. Finally, they theoretically used finite element modeling and molecular simulations to



understand such behavior. They found graphene sheets with defects were more rugged and structurally robust than previous results. Very sensitive thermal and electrical transport in graphene is observed for disruptions in the  $sp^2$ -bonding network. One significant result is that defective graphene's breaking strength is only 14% smaller than its new counterpart in the  $sp^3$ -defect regime.

Meanwhile, understanding the role of Cu vapor in the graphene growth process is essential to developing a reliable synthesis method for high-quality graphene. However, only a few studies<sup>218,219</sup> examined the effects of Cu vapor on graphene growth. Lee *et al.*<sup>220</sup> investigated the effects of Cu vapor on the growth of CVD graphene on a Cu surface. They found that the high partial pressure of Cu vapor enlarges the graphene grains by reducing the surface concentration of the carbon adatoms that participate in graphene growth. Also, the presence of Cu vapor favors the selective etching of oxygen functionalized carbons in graphene, thus increasing the efficiency of healing graphene defects by  $CH_4$ . They claimed a higher charge carrier mobility of  $14\,700\text{ cm}^2\text{ V}^{-1}\text{ s}^{-1}$  than exfoliated graphene by continuously supplying Cu vapor during CVD. Since adatoms' properties are highly dependent on the adsorption configuration (*e.g.*, isolated *vs.* clustered), it is essential to understand these effects (configuration-dependent properties and migration) from a theoretical perspective and be able to test them experimentally.

## 2.6 Substitutional impurity defects

Substitutional impurities can be generated by incorporating foreign atoms so that the removal of a carbon atom creates a vacancy filled by a foreign atom. Substitutional doping of graphene is an efficient and widely used method to tailor graphene's electronic and magnetic properties. Foreign atom impurities are either metal or non-metal elements. In this case, the impurity atoms replace one, two, or more carbon atoms. For non-metal impurities, boron or nitrogen atoms are of considerable interest because impurities shift the position of the Fermi level and change the electronic structure of graphene.<sup>133</sup> Nitrogen and boron are commonly used as electron donors or acceptors in graphene because their atomic sizes are closer to carbon and readily fit the graphitic lattices.<sup>221,222</sup> The covalent bonds between the N or B atoms and neighboring C atoms ensure that doped graphene possesses long-term thermal and chemical stability. On the other hand, the migration of Au and Pt atoms, most likely at substitutional sites in graphene layers, has been the subject of an *in situ* study by electron microscopy.<sup>188</sup> Substitutional defects have been found in transition metal dichalcogenides in the electron beam irradiation process by introducing other atomic species into the TEM chamber. The local density of states shows that N, P, As, and Sb atoms behave as acceptors, whereas F, Cl, Br, and I atoms are likely to be donors. The isoelectronic atoms, such as O, Se, or Te atoms, did not produce any localized states, signifying that they could heal the electronic structure of transition metal dichalcogenides with chalcogen vacancies.<sup>223</sup>

Both experimental and theoretical studies reported that the heteroatoms (N, B, or S) could modify the electrical properties of graphene with efficient catalytic properties for oxygen reduction reaction (ORR) because of the polarized distribution of spin and charge densities by doped heteroatoms.<sup>34,224–230</sup> Because DFT is an effective method for studying the electronic properties of catalytic materials and ORR mechanisms, it was used to investigate the ORR mechanisms in various catalytic materials.<sup>231–233</sup> The ORR mechanisms on carbon-supported Fe or Co-phthalocyanine in alkaline media were also investigated. Prof. Lv and Prof. Yamada nicely explained nitrogen in graphene and graphene nanoribbons.<sup>234–236</sup> In particular, Prof. Lv shows a nice microscope image of the nitrogen-containing defects.<sup>234</sup> In the literature, Prof. Yamada summarizes the types of oxygen- and nitrogen-containing functional groups.<sup>235–237</sup> Chen *et al.*<sup>238</sup> performed DFT calculations to study the ORR mechanisms on graphene, nitrogen-doped graphene, and cobalt-graphene-nitride systems.<sup>232,239</sup> Bhatt *et al.*<sup>43</sup> comparatively investigated the ORR mechanisms on Al-doped X-graphene (X = N, P, and S) electrocatalysts in the acidic medium in a fuel cell cathode. They found that Al-doped N- and P-graphene sheets are energetically more favorable than Al-doped S-graphene catalysts for enhanced and stable ORR *via* four-electron transfer pathways in an acidic environment. Prof. Nakamura and Prof. Ozaki also investigated ORR in nitrogen-doped carbon materials for fuel cell applications.<sup>240–243</sup> Using STM, Zhao *et al.*<sup>244</sup> reported images of individual nitrogen atoms doped in monolayer graphene. Measurements using X-ray photoelectron spectroscopy and near-edge X-ray absorption fine structure spectroscopy confirmed the presence of N dopants in graphene lattices as well as the formation of in-plane N–C bonds, indicating that the nitrogen atoms were substituted into the graphitic matrix. STM images (Fig. 5a) and simulations (Fig. 5b) reveal that a fraction of the extra electrons of the nitrogen atom delocalized into the graphene lattice, leading to the triangular shape of the individual N dopant sites. Because STM is sensitive to DOS near the Fermi level, resolving the atomic structure of topological defects involving delocalized electrons remains difficult. Marangoni *et al.*<sup>245</sup> synthesized an N-doped chevron GNR (cGNR) decorated alternatively with electron-rich carbazole groups (pentagon) and electron-deficient phenanthridine (hexagon) at the convex protrusions of the cGNRs, as shown in Fig. 5c and d. Previous research found substitutional Ni impurities in single-walled carbon nanotubes (SWCNT) and graphitic particles.<sup>246</sup> Ushiro *et al.*<sup>247</sup> reported that Ni substitutional defects are present in SWCNT samples even after careful purification. According to their analysis of the X-ray absorption data, the most likely configuration was the one in which the Ni atom replaces a carbon atom, as shown in Fig. 5e,<sup>41</sup> and four nitrogen doping configurations usually observed on graphene catalysts.<sup>248</sup>

Substitution of magnetic transition metals is also expected to strongly affect the magnetic properties of graphene nanostructures. For example, transition metals like Fe, Ni, or Co are among the most common catalysts used to produce SWCNT.<sup>249</sup> Rodriguez-Manzo *et al.*<sup>251</sup> also investigated the possibility of creating individual vacancies at desired locations in carbon nanotubes using electron beams. When combined with the



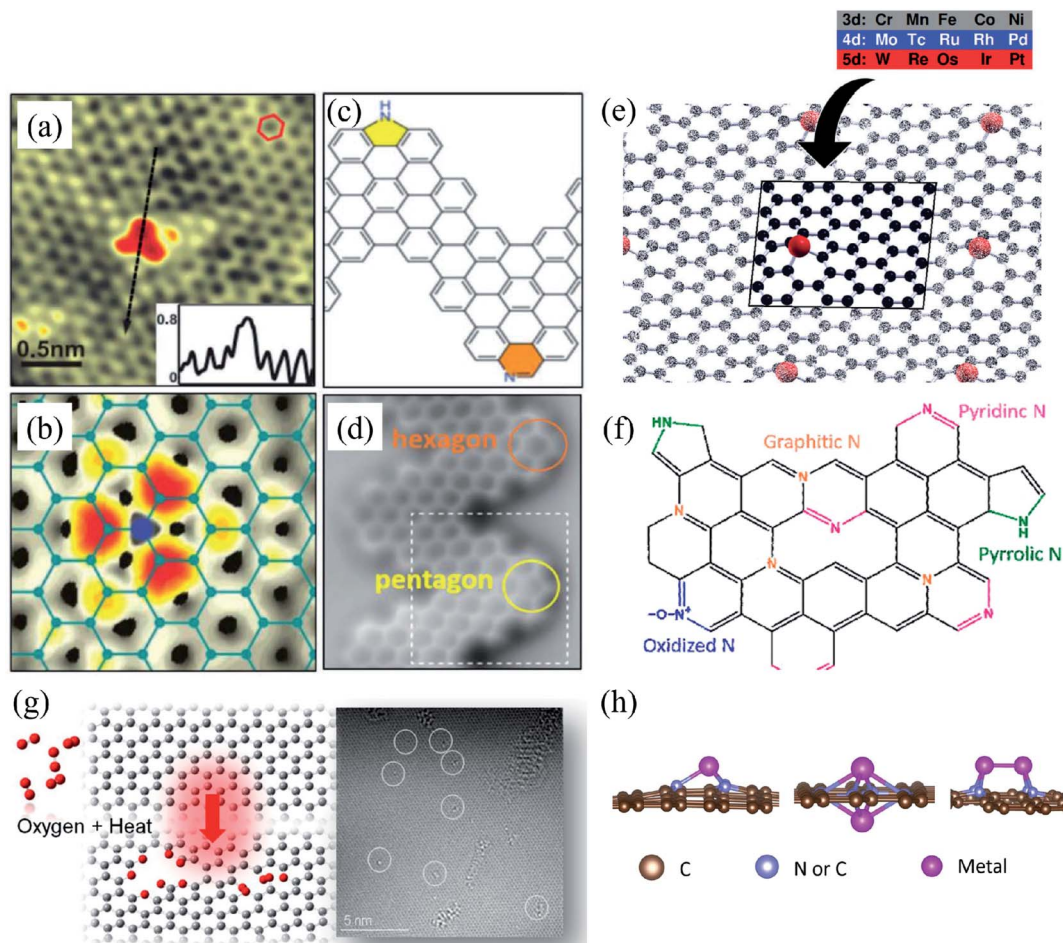


**Fig. 5** Substitutional doping of graphene and graphene nanoribbons: (a) STM image of graphene on copper foils with a single graphitic N dopant and (b) simulated STM image of graphene with a single graphitic N dopant. Reproduced with permission from ref. 244. Copyright 2011 American Association for the Advancement of Science; (c) schematic of nitrogen-doped chevron GNR with highlighted carbazole (yellow) and phenanthridine (orange) rings and (d) Nc-AFM image of a cGNR on Au (111) with the phenanthridine and carbazole groups highlighted with yellow and orange rings. Reproduced with permission from ref. 245. Copyright 2016 Wiley-VCH; (e) typical geometry of transition 3d, 4d, and 5d substitutional metal atoms in graphene. Reproduced with permission from ref. 41. Copyright 2016 Royal Society of Chemistry; (f) four nitrogen doping configurations usually observed on graphene catalysts. Reproduced with permission from ref. 249. Copyright 2018 <https://www.mdpi.com/journal/catalysts>; (g) HRTEM images of pristine graphene and oxidized graphene after 5 hours of oxidation at 493, 513, and 533 K. Reproduced with permission from ref. 250. 2014 American Chemical Society; (h) side views of relaxed structures of a single TM ( $M = \text{Fe, Co, Ni, or Cu}$ ) atom and TM ( $M_1 \text{ or } M_2 = \text{Co, Fe, Ni, or Cu}$ ) pairs with antisymmetric and symmetric forms. C or N atoms are represented by blue balls in the schematic diagram. Reproduced with permission from ref. 248. Elsevier Ltd. 2021 Copyright.

observed stability of substitutional impurities, such an ability may provide a route to fabricating new devices incorporating substitutional impurities in certain locations or arranged in particular ways. Si impurities can further pick up various atoms from the environment. Recent experimental studies have reported the presence of individual defects formed by the occurrence of silicon and nitrogen impurities.<sup>252,253</sup> Zhou *et al.*<sup>252,253</sup> showed that surface plasmons are locally enhanced at silicon and silicon-nitrogen impurities. Therefore, in principle, such silicon impurities in graphene could be used as plasmonic waveguides with potential applications in optoelectronic devices.<sup>254</sup> Electronic transport in systems with silicon point defects has been studied in ribbon geometry.<sup>255</sup> In addition, Cheng *et al.*<sup>256</sup> studied the electronic and transport properties of the  $\text{SiN}_x$  defects in armchair nanoribbons. However, it is

unclear about the transport properties of realistic two-dimensional graphene systems with numerous randomly positioned defects. Ervasti *et al.*<sup>257</sup> reported that many nitrogen-doped silicon impurities exhibited finite spin moments with graphene-based spintronics applications and evaluated the spin-dependent electronic and transport properties of the most stable defects. The doping of graphene with transition metals and their spintronics applications is underway. Thus, the study of magnetic substitutional impurities is vital for a theoretical understanding of magnetism for atomic defects in graphene and for explaining experiments in progress that dope graphene with elements of the traditional magnetic bulks (Fe, Co, and Ni). Previously, substitutional 3d transition metal atoms in a graphene layer were computed, and a simple model was proposed to explain their bonding and magnetism.<sup>190,258</sup> Some researchers



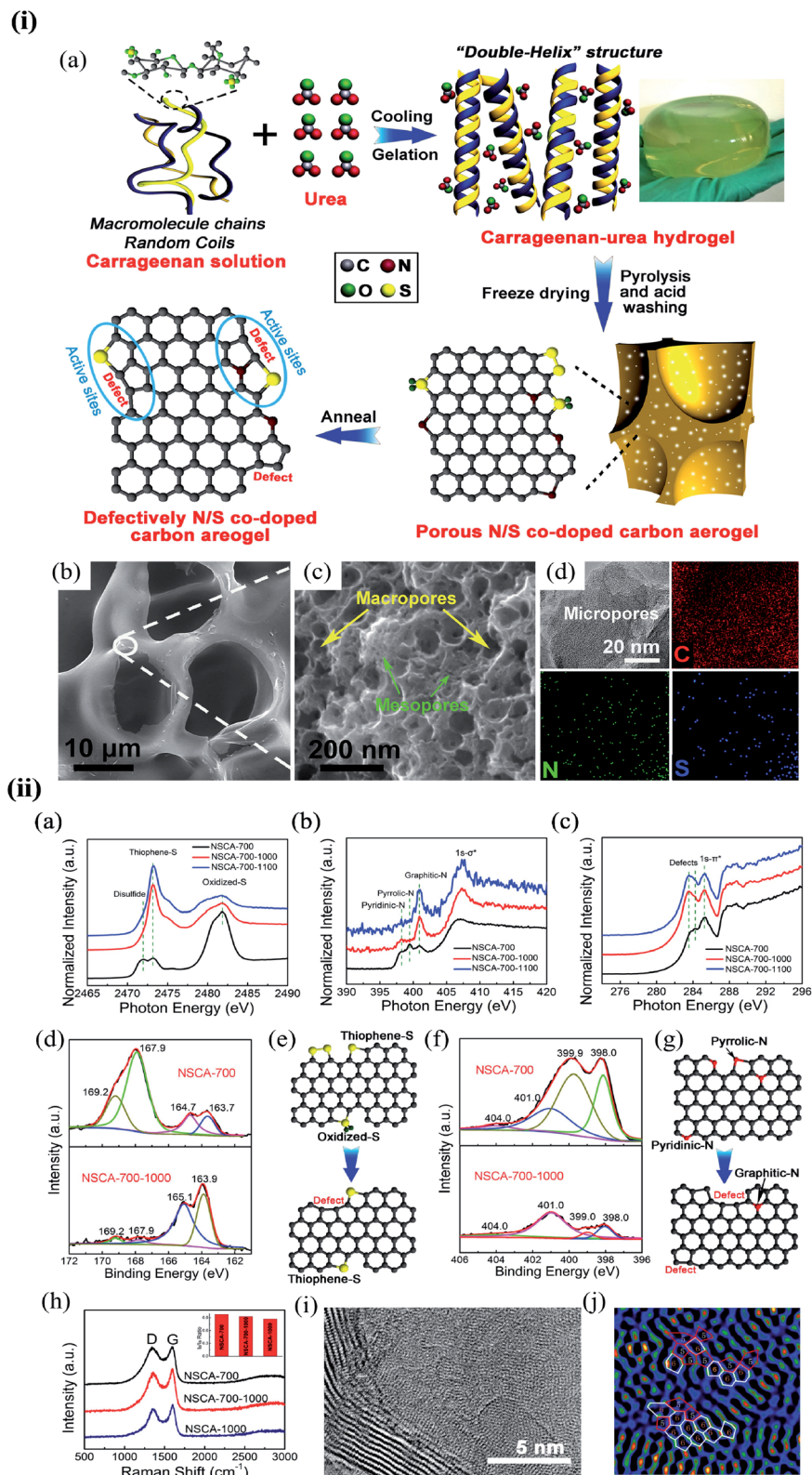


**Fig. 6** (i) The synthesis process and morphology of N-modified S-defect carbon aerogel: (a) schematic illustration of the synthesis process; (b and c) low-resolution (b) and high-resolution (c) FESEM images of NSCA-700-1000 and (d) TEM image and the corresponding EDS mapping for C, N, and S elements of NSCA-700-1000. Reprinted with permission of ref. 266. Copyright 2018 Elsevier Inc. (ii) Characterization of NSCA: (a–c) S K-edge (a), N K-edge (b), and C K-edge (c) XAS spectra of NSCA-700, NSCA-700-1000, and NSCA-700-1100. (d and f) The high-resolution XPS spectra of NSCA: (d) S 2p and (f) N 1s. (e and g) Schematic illustration of the conversion of the heteroatom dopant through annealing treatment: (e) S dopant and (g) N dopant. (h) Raman spectra of NSCA-700, NSCA-700-1000, and NSCA-1000. (i and j) STEM (i) and the corresponding filtered images (j) of NSCA-700-1000. Reprinted with permission of ref. 266. Copyright 2018 Elsevier Inc.



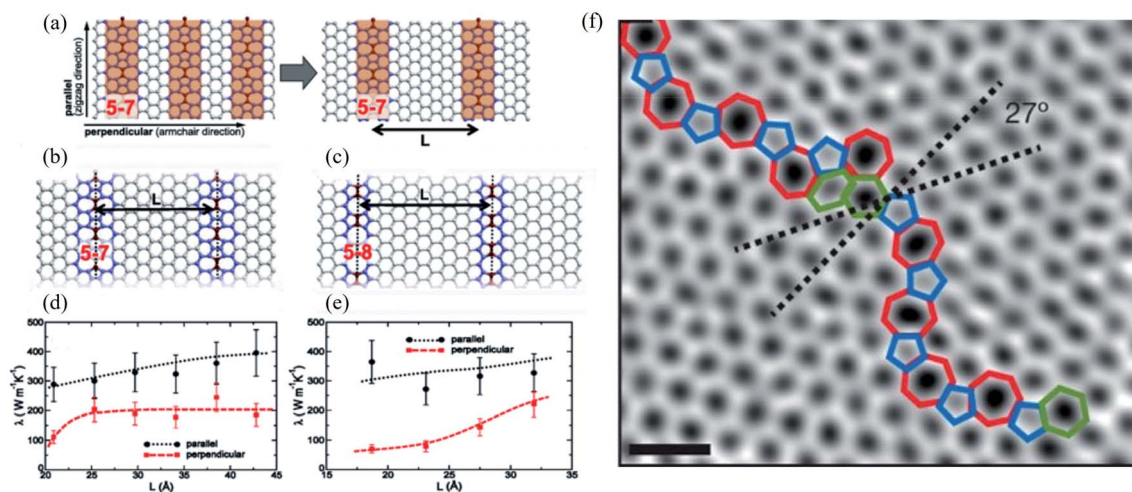


Fig. 7 Effect of line defects on thermal conductivity of a graphene monolayer: (a) arrangement of 5–7 defect lines; equilibrium structures of (b) 5–7 and (c) 5–8 defect lines; thermal conductivity  $\lambda$  of the system with (d) 5–7 and (e) 5–8 line defects as a function of their separation  $L$  at  $T = 300$  K. Reproduced with permission from ref. 276. Copyright 2014 American Physical Society. (f) Aberration-corrected annular dark-field scanning transmission electron microscopy (ADF-STEM) of line defects in graphene; scale bars: 5 Å. Reprinted with permission from ref. 269. Copyright 2010 Nature Publishing Group.

claimed that the ORR active sites are the M–N<sub>x</sub> impurities in M–N<sub>x</sub>/C catalysts.<sup>259,260</sup> He *et al.*<sup>261</sup> reported the performance of MN<sub>x</sub>/C in the order of FeN<sub>x</sub>/C < CoN<sub>x</sub>/C < NiN<sub>x</sub>/C < CuN<sub>x</sub>/C.<sup>260,262</sup> They suggested that O<sub>2</sub> and OH adsorption energies represent the ORR catalytic activity and stability for MN<sub>x</sub>/C electrocatalysts. Zhang *et al.*<sup>263</sup> performed both experimental and DFT investigations on transition metal (Fe, Co, Ni, Cu) phthalocyanines as electrocatalysts for ORR and concluded O<sub>2</sub> and OH adsorption energies as the catalytic activity and stability, while H<sub>2</sub>O<sub>2</sub> desorption energy as the number of electrons transferred in ORR processes. Bhatt *et al.*<sup>264</sup> performed DFT calculations to investigate the ORR mechanisms on M–N<sub>2</sub>–G (M = Ti, Cu, Mo, Nb, and Ru) catalysts and found that M–N<sub>2</sub>–G (M = Ti, Cu, Mo, Nb, and Ru) catalyst surfaces are energetically favorable (exothermic) for ORR through 4-electron transfer pathways to form two water molecules. However, the Cu–N<sub>2</sub>–G catalyst surface facilitates the formation of unwanted hydrogen peroxide through two-electron transfer pathways. Li *et al.*<sup>265</sup> very recently investigated both the ORR and oxygen evolution reaction (OER) catalytic activities of zinc and nitrogen co-doped graphene with different zinc–nitrogen (Zn–N) coordination numbers and configurations and found that both Zn–N coordination numbers and structural configurations influence the ORR and OER activities on ZnN<sub>x</sub> sites. They concluded that the O-p orbital shows moderate hybridization strength with the N-p and Zn-d orbitals in O-adsorbed ZnN<sub>4</sub> systems, thus facilitating electrocatalytic reactions. The vacancy defects have been introduced by heat-treating graphite oxide<sup>253</sup> and graphene under oxygen in the literature.<sup>254</sup> A schematic diagram of single and two metal atoms on graphene is shown in Fig. 5h.<sup>248</sup> Li *et al.*<sup>266</sup> investigated a metal-defect-free electrocatalyst-driven oxygen reduction reaction in acid electrolyte using experimental and computational methods. Their results reveal that the pentagonal S defect is essential for the ORR in acidic electrolytes

because it remarkably increases reactivity. One graphitic-type N in the meta-position of the pentagon defect further significantly improves the reactivity due to locally precise control of the electronic structure, thus forming highly active sites for ORR in acid. Fig. 6 shows the synthesis process and the morphology with active sites.<sup>266</sup>

A schematic illustration of the synthesis process is shown in Fig. 6i(a). Field emission scanning electron microscopy (FESEM) images show that all the samples have a 3D self-supporting core network structure (Fig. 6i(b)). Small-sized macropores and mesopores with interconnected structures can be observed in the wall of the network (Fig. 6i(c) NSCA-700-1000)), delivering a large specific surface area. The porous structure and high surface area can supply a high density of exposed active sites and promotes mass transport. Transmission electron microscopy (TEM) – energy dispersive X-ray spectroscopy (EDS) elemental mappings show that the doped S and N atoms partially remain in the carbon aerogels after annealing at 1000 °C (Fig. 6i(d)). S K-edge X-ray absorption structure (XAS) spectra indicate that NSCA-700-1000 and NSCA-700-1100 mainly contain thiophene S as the dibenzothiophene-like structure (2473.3 eV). Oxidized S (2481.8 eV) and disulfide (2472.0 eV) structures in NSCA-700 were removed or transformed into thiophene S (Fig. 6ii(a)).

## 2.7 One- and two-dimensional defects (topological defects)

The concept of dislocations is based on 1D line defects. Grain boundaries or stacking faults are 2D defects. Besides, various types of edge terminations exist in 2D materials, and applying strain can also modify the structure of graphene. Such defects in the bilayer and multilayer graphene are also essential. A one-dimensional defect has been observed in several experimental studies of graphene.<sup>72,73</sup> Some of them in graphene resemble dislocations in a conventional crystal. However, the traditional



concept requires a Burgers vector and a dislocation line, which only appear in a three-dimensional crystal.<sup>1</sup> Various 1D or 2D defects will be discussed in the following sessions.

**2.7.1 Line defects.** In the 1940s, scientists explained how materials could deform plastically *via* atomic-scale line defects called dislocations. These defects can be understood as tiny carpet folds that allow one part of a material to move relative to another without expending much energy. The randomness of graphene growth by CVD leads to different crystallographic orientations in other locations. In graphene, two 5–7 pair defects with lower total energy are more stable than a local haeckelite structure (555–777) and become dislocation line defects.<sup>108</sup> Generally, line defects are tilt boundaries separating two domains of different lattice orientations with the tilt axis normal to the plane. Such defects can be considered a line of reconstructed point defects with or without dangling bonds.<sup>267,268</sup> Line defects in graphene frequently separate domains of different crystal orientations. Several examples have been shown in the growth of graphene on metal surfaces.<sup>69,105</sup> As a result, a line defect appears when two graphene grains with differing orientations coalesce. The grain boundary structures observed in CVD graphene include lines of 5–7 defects on Cu<sup>269</sup> and 5–8 defects on the Ni (111) surface.<sup>69</sup> There is strong evidence that thermal transport in graphene is adversely affected by isotopic and structural impurities, including monovacancies, Stone–Thrower–Wales defects, and line defects.<sup>270–275</sup> The theoretical thermal conductivity of graphene modified by a periodic array of defect lines in Fig. 7a–c, both parallel and perpendicular to the defect lines, is shown in Fig. 7d and e.<sup>276</sup> Fig. 7f shows the aberration-corrected annular dark-field scanning transmission electron microscopy (ADF-STEM) graphene line defect, in which the two crystals are stitched together predominantly by a chain of pentagons, heptagons, and hexagons.<sup>269</sup> Z. G. Fthenakis *et al.*<sup>276</sup> concluded

that the precise nature of the structural defect<sup>271</sup> plays a minor role in determining the phonon scattering.

Line defects, including grain boundaries and wrinkles, are commonly seen in graphene grown by CVD, which is believed to alter the graphene's electrical and mechanical properties. Unfortunately, it is challenging to directly distinguish grain boundaries from wrinkles because of their similar morphologies. Long *et al.*<sup>277</sup> reported high-resolution Kelvin potential force microscopy (KPFM) to measure the work function distribution of graphene line defects and found the different work functions of grain boundaries, standing-collapsed wrinkles, and folded wrinkles. They concluded that the unique work function distribution of each type of line defect originated from the doping effect induced by the SiO<sub>2</sub> substrate using classical and quantum molecular dynamics simulations. Ramiro Marcelo dos Santos *et al.*<sup>278</sup> recently investigated the effects of the different numbers of line defects of substitutional nitrogen or silicon atoms on the penta-graphene electronic behavior. They found that such doping can induce semiconducting, semi-metallic, or metallic behavior depending on the doping atom and targeted hybridization (sp<sup>2</sup> or sp<sup>3</sup>-like carbons). They concluded that nitrogen doping of sp<sup>2</sup>-like carbon atoms could produce a bandgap modulation between semi-metallic and semiconducting behavior.

Recent STM measurements have shown that the o–p line defect exhibits excellent electronic properties.<sup>69,279</sup> However, its mechanical properties are largely unknown.<sup>280</sup> Substitutional nitrogen doping has been done *via* CVD or electrochemical treatment.<sup>281–283</sup> The effect of nitrogen doping on the electronic properties of pristine or point-defected graphene has been widely studied from both the experimental and computational sides [241, 311–313].<sup>221,283–286</sup> However, few studies have addressed doping in extended line defects.<sup>287,288</sup> Brito *et al.*<sup>288</sup> have shown that nitrogen doping is more favorable near a line

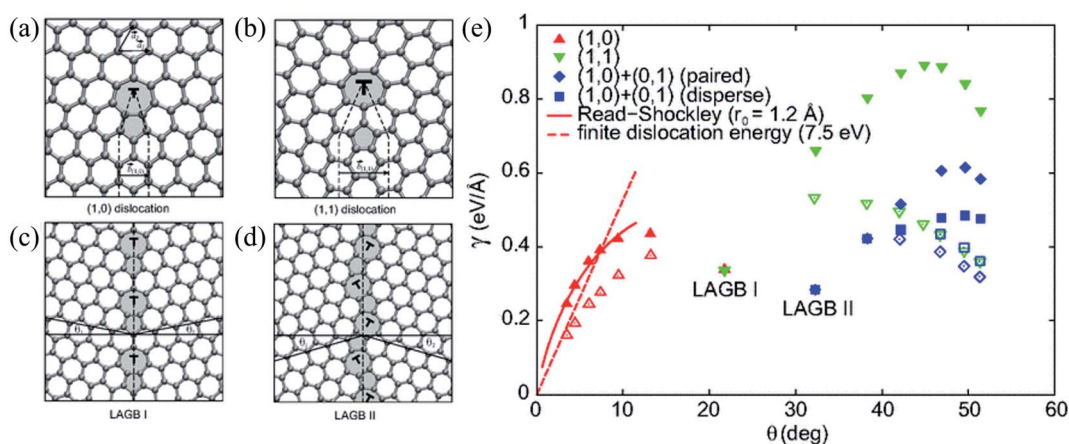


**Fig. 8** (a and b) Atomic structures of (1, 0) and (1, 1) dislocations. The dashed lines delimit the semi-infinite strips of graphene introduced at the dislocation core. Non-hexagonal rings are shaded. (c and d) Atomic structures of the  $\gamma = 21.81$  (LAGB I) and the  $\gamma = 32.21$  (LAGB II) symmetric large-angle grain boundaries, respectively. The dashed lines show the boundary lines and the solid lines definite angles  $\gamma_1$  and  $\gamma_2$  ( $\gamma = \gamma_1 + \gamma_2$ ) defining orientations of the graphene grains. (e) Grain-boundary energy per unit length  $g$  as a function of misorientation angle  $\gamma$  for various flat (filled symbols) and buckled (open symbols) grain-boundary structures. The two energetically favorable large-angles grain boundaries, LAGB I and LAGB II, are labeled. The dashed curves show the asymptotic linear dependence of  $g$  for the buckled small-angle armchair grain boundaries ( $E_f = 7.5$  eV). Reprinted with permission from ref. 299. Copyright 2010 American Physical Society.



defect than in the graphene region based on formation energies using DFT. Berger *et al.*<sup>289</sup> addressed the effects of nitrogen and boron doping on the electronic and mechanical properties of h-p and o-p line defects in graphene employing full-potential DFT by investigating the fact that doping primarily affects the occupation of the frontier orbitals, *i.e.*, occupation through n-type doping or local substitution with nitrogen increases the ultimate tensile strength remarkably. What will happen in the presence of two or more line defects? Motivated by finding an efficient realization of the high valley polarization, Liu *et al.*<sup>290</sup> studied the electron transmission coefficient in the presence of several line defects. They discovered a noticeable change in

transmission coefficients with varying distances between two-line defects with temperature insensitivity. Polarization could be used for information processing much as the electron spin degree of freedom is used in spintronics, with the added benefit of temperature insensitivity. Two methods have been suggested for lifting the degeneracy and thus achieving graphene valley polarization: (i) by applying an external magnetic field and (ii) by modifying the lattice. The first method requires very high magnetic fields and low temperatures or optical pumping by circularly polarized light to generate and detect valley polarized currents. The second method is more compatible with modern electronic synthesis but requires a practical way of generating

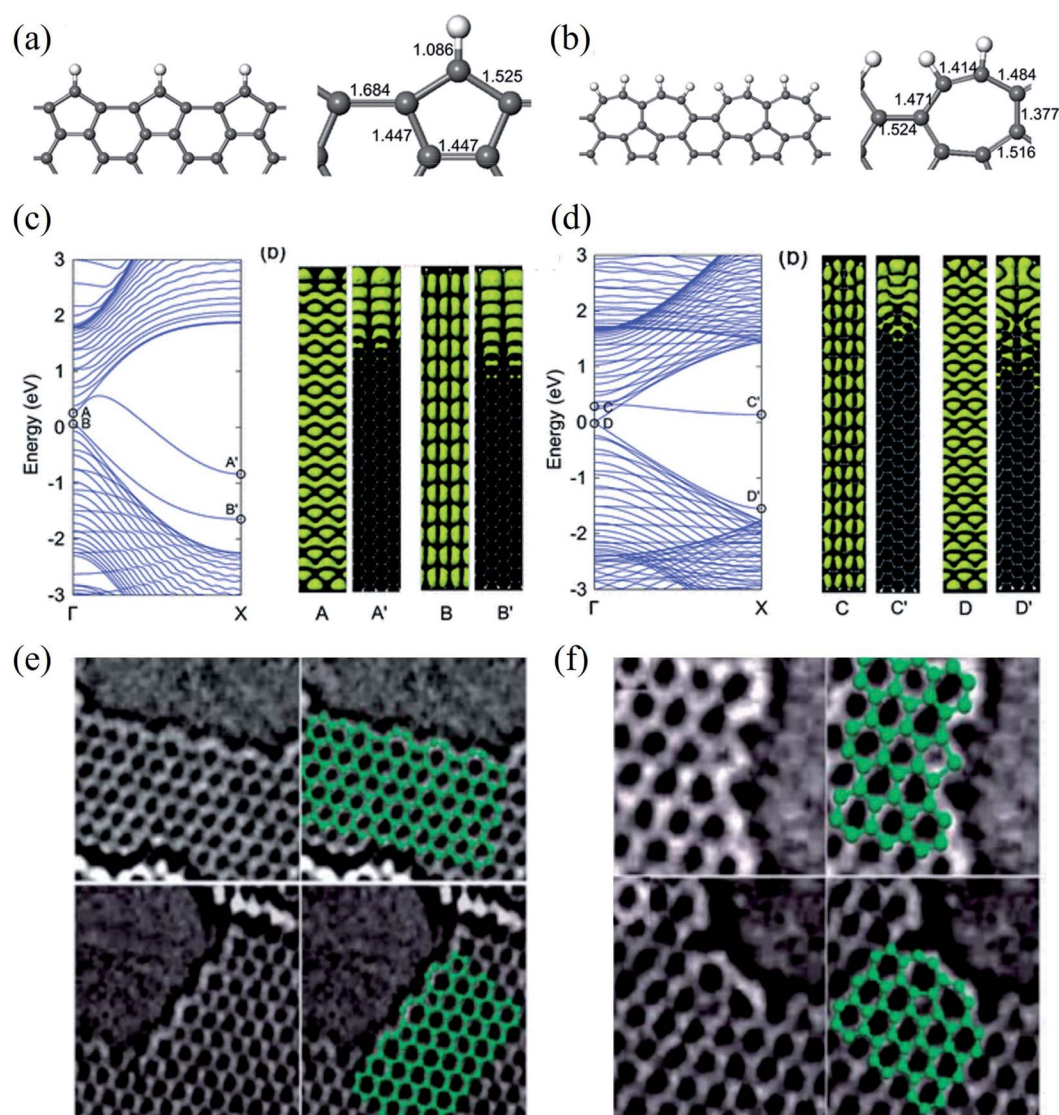


**Fig. 9** Relaxed geometries of reconstructed armchair graphene edges: (a) pentagonal armchair edge with missing carbon atoms [ac(56)] and (b) reconstructed armchair edge in which two heptagons created by the Stone–Wales transformation share a side [ac(677)]. The bond lengths (in Å) at the graphene edges are shown in the right panel. (c) Band structure of a GNR with an ac(56) edge (left panel), and electronic densities of two edge-related states (right panel). The labels A(B) and A'(B') indicate electronic densities in the same band at  $\Gamma$  and X, respectively. (d) Band structure of a GNR with the ac(677) edge (left panel), and electronic densities of two edge-related states (right panel). The labels C(D) and C'(D') indicate electronic densities in the same band at  $\Gamma$  and X, respectively. Reprinted with permission from ref. 329. Copyright 2008 American Physical Society. Experimental evidence of: (e) zigzag edge reconstruction and (f) armchair edge reconstruction. Reprinted with permission from ref. 332. Copyright 2009 American Physical Society.



functional atomic-scale structures and a compact scheme for operating the device.<sup>291–297</sup>

Remarkably, extended line defects induce charge redistribution in their surroundings and could thus behave as a metallic wire embedded in a graphene sheet.<sup>69</sup> As a result, when compared to isolated defects associated with electron scattering and heat generation,<sup>298</sup> such topological defects may improve graphene's electronic transport properties.<sup>107,279,280,299</sup> However, these properties generally depend on the relative orientation between the grain boundary and transport direction.<sup>300–302</sup> It was shown that the interaction between graphene and electron acceptor molecules increases the device's conductivity. In contrast, electron donors induce a decrease in conductivity, which has also been experimentally observed for various molecules.<sup>303–308</sup> Nonetheless, the interaction between graphene and closed-shell molecules tends to be relatively weak, implying a low signal-to-noise ratio. Zhang *et al.* investigated whether the sensitivity of graphene-based nanosensors could be improved by introducing dopants or vacancies.<sup>309,310</sup> However, such an improvement to graphene-based gas sensors comes at the cost of significantly larger adsorption energies of the target molecules and, consequently, an increase in recovery time. Hence, a suitable sensor should have three essential features: (i) a small but not negligible binding energy, (ii) significant sensitivity, and (iii) significant selectivity to different gases.<sup>311–313</sup>

**2.7.2 Grain boundaries defects.** The pairs of pentagons and heptagons or those of pentagons and octagons are expected to form at grain boundaries (GBs).<sup>314</sup> Fig. 7f shows two graphene grains connected with a relative misorientation of  $27^\circ$  and are stitched together by a series of pentagons, heptagons, and distorted hexagons, forming a tilt boundary.<sup>269</sup> The non-hexagonal rings in polycrystalline graphene play an essential structural role as grain boundaries between arbitrarily oriented graphene flakes. Dislocations characterized by any Burgers vector as well as grain boundaries, covering the whole range of possible misorientation angles, can be constructed based on coupled ((1, 0) dislocation) and dissociated ((1, 1) dislocation) 5–7 pairs separated by hexagons (Fig. 8).<sup>299</sup> Recent atomic-resolution TEM studies reported the observation of GBs in CVD-grown graphene.<sup>69,113,269,315</sup> The experimental studies have shown that the GBs are not perfectly straight lines in general and that the sets of pentagon–heptagon defects along the boundaries are not periodic. These extended pentagon–heptagon defect lines intercept each other at random angles, forming irregular polygons with edges showing a stochastic distribution of lengths. Theoretical studies have argued that GBs strongly affect graphene's chemical, mechanical, and electronic properties.<sup>268,299,316</sup> Electronic mobilities of films produced through CVD are lower than those reported on exfoliated graphene because electronic transport is hindered by grains and GBs.<sup>3,107,317–320</sup> Recently, some theoretical studies concentrated on the scattering and transport properties of an extended linear defect acting as a one-dimensional conducting charged wire using the tight-binding (TB) model.<sup>69,291,321,322</sup>

**2.7.3 Edge defects.** Different kinds of edge terminations exist in 2D materials, which directly determine the

morphologies and properties of 2D materials. Each graphene layer is terminated by the edge atoms being either free or passivated with hydrogen atoms. The mechanically exfoliated graphene sheets have crystal cleavage behaviors.<sup>323</sup> Experimentally, various graphene edges have been fabricated and characterized by different techniques. Among them, edges along the zigzag (ZZ) or armchair (AC) direction are more frequently observed. The edge of 2D graphene, as the surface of a 3D crystal, plays a crucial role in determining its physical and chemical properties and thus has been extensively studied recently. Graphene edges are very reactive and are affected by the ribbon width and the orientations of C atoms at their edges. Graphene nanoribbons (GNRs) are more reactive than bulk single graphene sheets. Zigzag GNRs (ZGNRs) show higher chemical reactivity than armchair GNRs (AGNRs). ZGNRs have higher chemical reactivity due to unpaired electrons on their edges. Theoretical studies predict that ZGNRs are metallic and have certain localized edge states, antiferromagnetically coupled between the two edges, while AGNRs are nonmagnetic and semiconducting. As a result, the edges of GNRs play a vital role in modulating their electronic properties. Structural modification of the edges, such as bond reconstruction, edge functionalization, passivation, doping, and strain, leads to alteration of the  $\pi$ -network at the edges. These structural modifications are potential methods to tailor the geometries, stability, electronic properties, spin polarization, spin gap asymmetry, and size of the graphene bandgap. Various atoms and chemical groups have been used to functionalize the graphene edges.<sup>31,324–328</sup> Besides, hydrogen atoms and other chemical groups that can saturate dangling bonds at the edge under ambient conditions may be considered a disorder, dramatically increasing the number of possible edge defects. For example, an edge defect is the removal of a carbon atom from a zigzag edge, which leads to a pentagon in the middle of a row of hexagons at the edge, and other edge reconstructions result in different combinations of pentagons and heptagons at the edge, namely ac(56) and ac(677), as shown in Fig. 9a and b.<sup>329</sup> The unit cell size of the ac(677)-type edge was considered twice that of the ac(56)-type edge along the graphene nanoribbon axis. In Fig. 9a and b, all geometries are strictly in-plane. Fig. 9c and d show the electronic band structure and charge densities at  $\Gamma$  and X in the armchair GNR with ac(56) and ac(677), respectively. The electronic bands near the Fermi level labeled AA' and BB' (Fig. 9c) and CC' and DD' (Fig. 9d) appear in the forbidden band. At the zone boundary (X), the edge states existed as deep levels, so they were more localized than the edge states at the  $\Gamma$  point.<sup>329</sup> It was reported that the edge hopping energy  $t$  was  $-2.0$  eV (ref. 330) using the maximally localized Wannier function method<sup>331</sup> for boundary softening in ideal graphene. The edge formation shown in Fig. 9e and f has direct experimental evidence of the pristine graphene edge's reconstruction, including the observation of both zz(57) and ac(677).<sup>332</sup> Such spontaneous edge reconstructions have also been discussed in ref. 333 and 334, and experimentally identified in ref. 115.

Therefore, to better understand the edge effects on the band structure of GNRs theoretically, one should either develop more



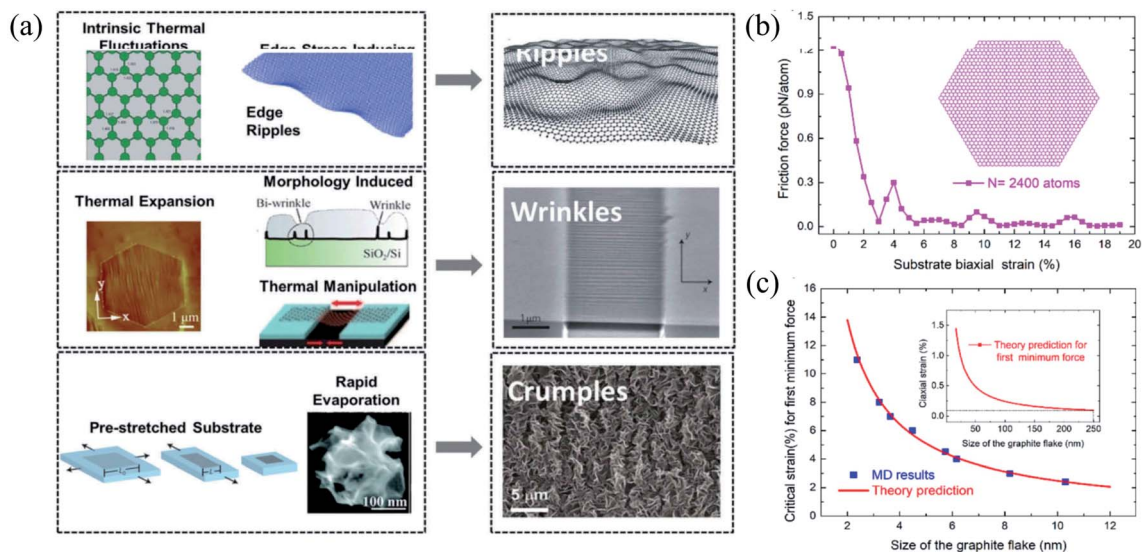


Fig. 10 (a) Three types of corrugations: ripples, wrinkles, and crumples. Reprinted with permission from ref. 372. Copyright 2015 they published by Elsevier Ltd. (b and c) Size effects of the flake on friction under different biaxial stretching strains in the substrate: (b) flake containing 2400 atoms and (c) MD simulations *versus* theories of the critical strain for first minimum friction. Reprinted with permission from ref. 385. Copyright 2019 the American Chemical Society.

accurate calculations than those for standard ZGNRs and AGNRs<sup>20,335</sup> or consider the real structure of the edges.<sup>329,332,336</sup> The edge defects in graphene nanoribbons were observed *via* Raman spectra,<sup>337,338</sup> STM,<sup>339</sup> and high-resolution electronic transmission microscopy.<sup>115,340,341</sup> The edge disorder leads to the conduction gap in the GNRs.<sup>342</sup> Li *et al.*<sup>343</sup> reported that the current–voltage characteristic is reduced in vacancy on the edge of ZGNR and induces the conductance gap near the Fermi energy using DFT. The edge disorder leads to the metal–semiconductor transformation in the ZGNR. However, it changes the properties of AGNRs slightly.<sup>344</sup> On the other hand, the GNRs are affected by the dephasing process because of thermal environmental fluctuations and electron–electron interaction. As a result, decoherence transport is needed to obtain realistic results.<sup>345</sup> The Büttiker probe model<sup>346</sup> or self-consistent Born approximation<sup>347</sup> can use the dephasing scattering processes in non-equilibrium Green function formalism. It is well known that the surface plasmon resonance frequency in GNRs is a function of the width and the carrier density of the ribbons.<sup>348</sup> Although challenging to characterize at the nanoscale, the inactive edge has been evidenced by Raman spectroscopy<sup>349</sup> and microwave atomic force microscopy<sup>350,351</sup> to show different characteristics than in the basal plane. In addition, Fei *et al.*<sup>352</sup> also reported that the carrier density is enhanced near the sample edge using near-field infrared nanoimaging in exfoliated graphene. The patterned graphene edges have profound effects on doping, scattering, and plasmon reflection, presumably caused by edge defects and roughness<sup>353</sup> using the lithographically patterned CVD technique. Edge states introduced on GNRs using lithography constantly change the background charge density.<sup>354</sup> Therefore, graphene edges are assumed to be efficient doping centers through the passivation and functionalization of the edges.<sup>355</sup> The effect of the vacancy edge defect

(bonds breaking between carbon atoms) of a graphene sheet on the Raman spectrum was studied by Ten *et al.*,<sup>356</sup> and they found common changes in the Raman spectrum for the presence of nitrogen and oxygen atoms. A steric effect decreased the stretching vibration  $q$  (CH) frequency, which appeared in  $2700\text{ cm}^{-1}$  and corresponded to the 2D vibration. The vacancy edge defect modeling results for the nitrogen-doped graphene sheet fragment functionalized by oxygen atoms were compared with experimental TEM data.<sup>113,115</sup>

Moreover, Park *et al.*<sup>330</sup> investigated the roles of the pseudospin and the valley degeneracy in electron scattering at graphene edges using experimental techniques such as STM and theoretical analyses. They discovered that charge density modulations of short-wavelength oscillations and gradually decaying beat patterns strongly correlate with pseudospin and valley degeneracy. Furthermore, they claimed that the armchair edge exhibits nearly perfect intervalley scattering with variation in pseudospin. In contrast, the zigzag edge shows intervalley scattering only with the change in pseudospin orientation. They also simulated the armchair edge with pentagons<sup>332</sup> and found an atomic-scale node-like structure in the  $y$ -axis direction. The zigzag edge, however, was not found to have a periodic modulation like a node.

**2.7.4 Strain.** Strain is often overlooked in the experimental synthesis of graphene because of surface corrugation of the substrate or lattice mismatch between the graphene layer and substrate.<sup>357</sup> Thermal effects have been observed to deviate graphene from planarity in experimental and theoretical studies.<sup>358,359</sup> The asymmetric distribution of C–C bond lengths resulting from the localized electrons forces the graphene lattice to become non-planar to minimize free energy, thus forming ripples or buckles with heights of up to 1 nm. Therefore, thermal fluctuations induce ripples in intrinsic features of



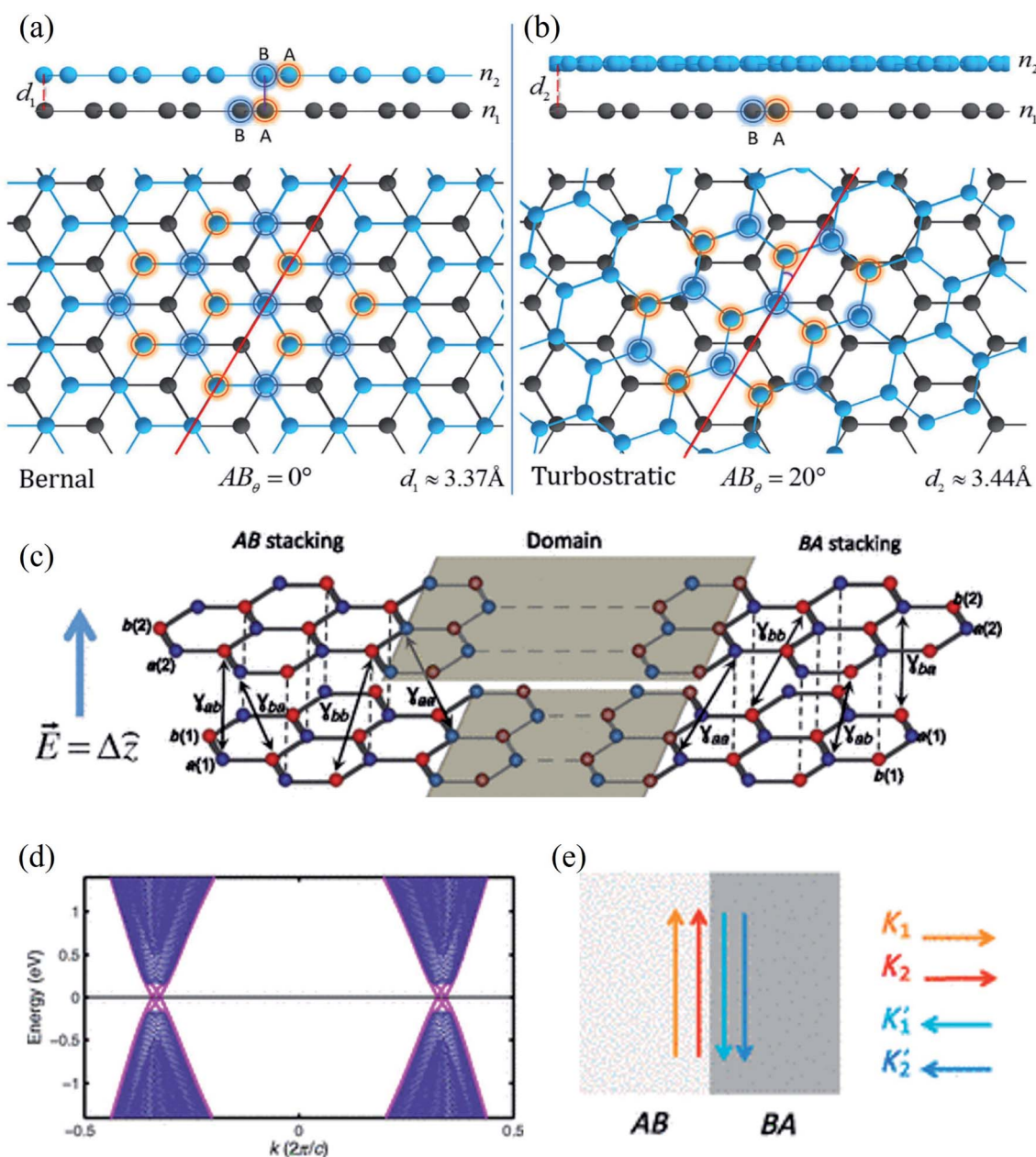


Fig. 11 (a) Bernal phase, or AB stacked, BLG and (b) turbostratic-stacked BLG. Reprinted with permission of ref. 424. Copyright 2020 Nature publishing group. (c) A typical AB–BA stacked BLG under strain, (d) the resulting band structure, and (e) schematics of valley-momentum-locked edge states at a tilt boundary. Reprinted with permission from ref. 425. Copyright 2013 the American Physical Society.

graphene sheets. As observed under STM,<sup>360</sup> these spontaneous ripples on the suspended graphene are dynamic. In addition, ultrathin films with only dozens of layers were observed to be thermodynamically unstable unless they inherently constitute a part of 3D structures (e.g., a substrate with a matching lattice).<sup>361–363</sup> Indeed, partially decoupled bending and stretching modes can significantly stabilize the atomically thin film.<sup>364</sup> In addition to intrinsic strain, extrinsic strain can be created and tuned in graphene by different methods.<sup>365,366</sup> The strain can modify graphene's band structure and electronic properties, as reported by first-principles studies.<sup>366–368</sup> Graphene can be characterized by two types of strain: uniaxial and shear

strain. The strain shows different behavior on graphene depending on its edge, either zigzag or armchair. For example, the bandgap of AGNRs was dependent on their geometry and the applied compression, while the antiferromagnetic states of ZGNRs were found to improve with compression.<sup>366</sup> In the mechanical stress, the critical strain at which the formation of SW defects in graphene becomes thermodynamically favorable was computed as 6–9% (ref. 121 and 369–371) and 12–17% (ref. 369 and 371) in the zigzag and armchair directions, respectively. The reactivity and functionalization of graphene can be boosted by applying stress to it. DFT studies reported the possible adsorption of  $\text{H}_2$ ,  $\text{N}_2$ ,  $\text{NO}$ , and  $\text{CO}$  molecules on the strained



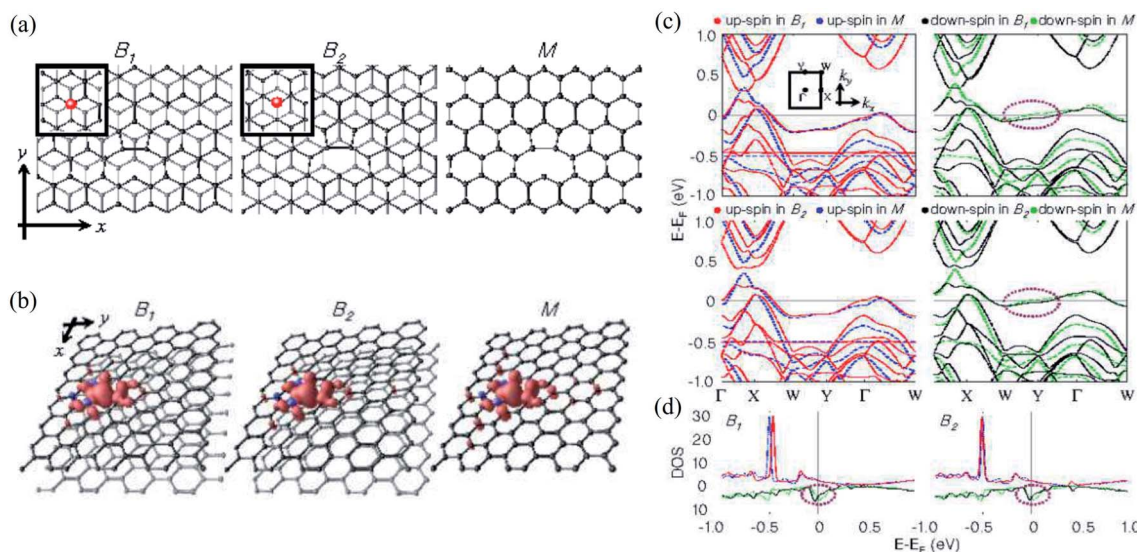


Fig. 12 (a) The relaxed structures, (b) spin density plots, (c) band structures and (d) DOS of upper layers of two types of Bernal-stacked graphene bilayers with a single vacancy ( $B_1$ ,  $B_2$ ) and graphene monolayers with a single vacancy ( $M$ ). Reprinted with permission from ref. 430. Copyright 2008 IOP Publishing Ltd.

graphene surface.<sup>368</sup> Wrinkles and crumples are the other types of corrugations in graphene sheets except for ripples (Fig. 10a).<sup>372</sup> Wrinkles are generally formed in metallic substrates because of the opposite thermal deformation and defect lines.<sup>373–375</sup> Crumples are dense deformations in 2D or 3D, generated by rapid evaporation.<sup>376</sup> Previous research found that friction between strained graphene and a diamond atomic force microscopy tip or silicon dioxide substrate decreases monotonically as stretching increases.<sup>377–381</sup> Several recent studies suggest that this monotonic reduction could also exist for graphene friction pairs with uniaxial or biaxial stretching strained on one of the surfaces.<sup>382–384</sup> Wang *et al.*<sup>385</sup> studied the effect of stretching strain (both uniaxial and biaxial) on the friction of graphene friction pairs using MD simulations. They found that the critical strain is required for a remarkable reduction in friction that decreases drastically with an increase in the size of the graphene flake, with a maximum size of more than 10 nm, as shown in Fig. 10c, and the underlying mechanism was supposed to be the evolution of moiré patterns. The critical strain corresponds to the first minimum in friction (3% strain), as shown in Fig. 10b. Although earlier studies<sup>386,387</sup> found that tiny uniaxial strains opened a gap at the Fermi level, subsequent studies<sup>367,388–393</sup> claimed that graphene remains gapless at small and moderate uniaxial strains up to a critical threshold deformation. The high failure limit of the strain was found to be about 25–27% in graphene for strain effects on the bandgap engineering of graphene.<sup>394–399</sup> Recently, Sahalianov and Radchenko investigated whether the bandgap in graphene can open *via* different types of lattice deformations.<sup>400–405</sup>

As a result, it does not show any piezoelectric behavior; however, several experimental and theoretical studies have shown the modification or engineering of graphene to achieve a piezoelectric response.<sup>406</sup> Wang *et al.*<sup>407</sup> reported the in-plane direct piezoelectric effect when in-plane biaxial strain is

applied using the AFM tip on graphene membranes across the supported/suspended graphene boundary, and band bending occurs because of biaxial strain. Graphene grown on metallic substrates often shows a periodic superstructure. Periodic height modulations have been measured in suspended graphene samples because of the mismatch between the expansion coefficients of graphene and substrate. Strains in suspended samples can be expected during the fabrication process. Many suspended samples show scrolls that induce significant curvatures and elastic strains.<sup>408</sup> Recently, Hsu *et al.*<sup>409</sup> reported an approach to manipulating the topological states by applying strain at room temperature and found an induced giant pseudo-magnetic field (up to  $\sim 800$  T) in strained graphene.

**2.7.5 Defects in bilayer and multilayer graphene.** Multilayer graphene layers are fabricated as a graphite-like structure by combining two or more graphene layers in a specific order. Their mechanical, optical, and electronic properties might be manipulated by varying the stacking order, interlayer spacing, and relative twisting angle.<sup>410–416</sup> Bilayer graphene consists of two stacked monolayers that may or may not be shifted towards each other in a stacked AB, or AA, or a twisted orientation, possessing an interlayer distance of 3.35 Å with the application of weak van der Waals interaction between the layers.<sup>417–419</sup> There will be no chemically bonded carbon atoms between the layers in pristine graphene. However, even in bilayer graphene, the defective graphene sheet layers will form new chemical bonds with adjacent carbon atoms because of intrinsic defects (holes, dangling bonds, or carbon atoms in the migrating state) in the graphene.<sup>420–423</sup> The structural defects will be more complex if the stacking process involves more graphene layers. As a result, graphene in different stacking regions must involve concurrent domain processes in constructing the graphite structure. The stacking of two monolayers of graphene with a specific twisting angle ( $\theta$ ) to get stacked bilayer graphene



(BLG) has been studied: namely Bernal-stacked BLG with  $\theta = 0^\circ$  and an interlayer distance of  $\sim 3.37 \text{ \AA}$ , and turbostratic-stacked BLG with  $\theta = 20^\circ$  and an interlayer distance of  $\sim 3.44 \text{ \AA}$  as shown in Fig. 11a and b.<sup>424</sup> A typical AB-BA stacked BLG under strain, the resulting band structure, and schematics of valley-momentum-locked edge states are shown in Fig. 11c-e.<sup>425</sup> In typical samples, the domain wall separating the AB- and BA-stacked domains has substantial width ranges 5–20 nm and the twisting angle ranges from  $0$ – $90^\circ$ .<sup>421</sup> The energy spectrum was plotted in Fig. 11d with the model parameters  $t = 2.8 \text{ eV}$  and  $\Delta = 0.5 \text{ eV}$ . The moiré pattern emerged with a higher periodicity.<sup>419,426</sup> A previous DFT study revealed that the migration barrier for monovacancy in turbostratic-stacked BLG is 9–14% higher than that in monolayer graphene, depending on the migration direction, while that of divacancy in BLG is almost the same as that in the divacancy of monolayer graphene. The non-planar distortion is small in the divacancy structure, and the upper or lower layer does not affect the SW-type bond rotation.<sup>427</sup>

Ochapski *et al.*<sup>428</sup> investigated the influence of the defect density in multilayer graphene sheets (prepared *via* CVD on Ni substrates) on Li intercalation at room temperature using X-ray photoelectron spectroscopy. They found that Li intercalation is independent of the amount of defect induced, and the edges of the graphene flakes are dominant sites for Li adsorption in multilayer graphene. Castro and co-workers<sup>429</sup> reported the occurrence of localized states at zigzag edges of N-layer graphene using the tight-binding method. They found the surface states in a single plane in monolayer graphene, finite-amplitude states over the two first or last layers of the stacked bilayer graphene, finite-amplitude states over three consecutive layers, *etc.* Multilayer graphene edge states were observed because of the next-nearest-neighbor interlayer hopping.

On the other hand, Choi *et al.*<sup>430</sup> investigated monovacancy-induced magnetism in graphene bilayers using DFT methods. Because of the interlayer charge transfer from the adjacent defect-free layer to the vacant layer, spin magnetic moments localized at the vacancy sites of two types of Bernal-stacked graphene bilayers with a monovacancy ( $B_1$ ,  $B_2$ ) decrease by about 10% more than those of a graphene monolayer with a monovacancy. The relaxed structures, spin density plots, band structures, and DOSs of the upper layers of  $B_1$ ,  $B_2$ , and M are shown in Fig. 12. The Bernal-stacked (AB-type) graphene layer with a single vacancy and a graphene monolayer with a single vacancy are shown in Fig. 12a. The spatial localization of spin densities near the vacancy site and their distributions with mirror symmetry with respect to the  $y$ -axis are shown in Fig. 12b. Magnetic moments of  $1.31$  and  $0.04 \mu_B$  were computed for  $B_1$ ,  $1.35$  and  $0.04 \mu_B$  for  $B_2$ , and  $1.52 \mu_B$  for M, respectively. The comparison of band structures among  $B_1$ ,  $B_2$  and M was shown in Fig. 12c. The DOSs of the upper layer in graphene bilayers with a single vacancy are shown in Fig. 12d. In Fig. 12c and d, the contributions of spin-up and spin-down electrons were represented by red and black for  $B_1$  and M and blue and green for  $B_2$  and M, respectively. The band structure showed the localized  $sp^2$  dangling bond states at an energy of  $\sim 0.5 \text{ eV}$  below the Fermi level and quasi-localized defect states pinned at the

Fermi level.<sup>430</sup> The DOSs revealed that the magnetic moments mainly originate from the localized  $sp^2$  dangling-bond states and the contributions of quasi-localized defect states are minor for all three systems considered. An experimental technique was presented to directly manipulate dislocations *in situ* nanoscale using scanning electron microscopy to measure fundamental properties such as line tension, defect interaction, and node formation in free-standing bilayer graphene based on stacking order (AB or AC).<sup>431</sup> Moon *et al.*<sup>432</sup> demonstrated a layer-engineered exfoliation technique for observing large-scale graphene (mm size) with selective thickness control and adjusting these exfoliated layers with different metal films *via* the spalling mechanism. Recently, the twisted or stacked bilayer (or multilayer) graphene has been attracted significant attention from both theoretical and experimental researchers because of its extraordinary optical<sup>433–436</sup> and electronic properties.<sup>437–443</sup> These studies shed light on understanding defect structures in graphene where the number of layers is greater than or equal to 2. It could be crucial to use graphene in nanodevice and nano-engineering techniques.

### 3. Summary and outlook

Most of the research on graphene is circumvented around its pristine form. However, inevitable structural defects during the production process affect mechanical, thermal, and electrical properties of graphene and graphene-based nanocomposites. It is hypothetical to obtain a pristine form of graphene because of the method of production, chemical and heat treatment, and electron and ion beam irradiation. Investigating the effect of these defects on graphene's mechanical, thermal, and electrical properties is crucial for fundamental research in nanodevices. For these reasons, researchers shifted their focus to exploring the effect of defects on graphene's mechanical and fracture properties. In addition, charge or spin imbalances between the sublattices of graphene because of its symmetry and zero bandgap characteristics can be created by its interaction with the substrate, which alters its electronic and magnetic properties caused by its modified lattice. Therefore, controlling its interactions with the substrate and the surrounding environment is not easy. Structural modification of the edges, such as bond reconstruction, edge functionalization, passivation, doping, and strain, also tailors the inherent properties of graphene. Moreover, the current focus of the field is on controlling the annealing processes to make defect-free graphene nanostructures. However, a subsequent stage will likely be to create single defects within perfect graphene deliberately (*e.g.*, a small pore, a single step in a zigzag edge, or replacing a single C atom with a Pt atom) with the same level of perfection, which may have several applications, from electronic devices to catalysis.

Many fabrication methods for graphene have emerged. However, various kinds of defects, such as vacancies, substitutional impurities, adatoms, and topological defects, are inevitably formed during the growth of graphene because of the imperfection of the graphene production processes. In addition, defects can also be intentionally incorporated into graphene by ion-beam irradiation or chemical treatments.



Although the defects in graphene can be helpful in some applications, such as enhancing chemical reactivity and generating magnetism, the defects in graphene can adversely affect thermal conductivity and reduce mechanical strength. Besides, the decrease in the transport properties of graphene has also been attributed to defects. As a result, the large-scale preparation of graphene films with minimal defects has been challenging for commercial applications.

Regarding divacancy's effect on graphene's thermal transport, only the 5–8–5 (two pentagons and one octagon) divacancy was studied. 10% of divacancy defects were reported to reduce the thermal conductivity of graphene by 80%, and the decrease in thermal conductivity of the zigzag graphene nanoribbon is more significant than that of the armchair type for high defect concentration. However, experimental results show that 5–8–5, 555–777 (three pentagons and three heptagons), and 5555–6–7777 (four pentagons, four heptagons, and one hexagon) divacancies are stable and familiar in graphene, and they can propagate in the structure or transform each other. Therefore, it is necessary to systematically study the effect of divacancies with different structures on the thermal transport properties of graphene. In addition, it was found that thermal conductance could be effectively regulated by controlling the orientation or changing the length of the embedded long chain. The decrease in thermal conductance is caused by the change in phonon dispersion and the scattering of defects. However, the influence of 48 extended line defects on the thermal transport properties of the zigzag graphene nanoribbon has not been reported. If we consider the general relevance of divacancies to charge transport in nanotubes, as well as the fact that the 555–777 structure is more stable in graphene than the 5–8–5, it is fascinating to know the answer to questions such as (i) is the 555–777 defect also the most stable configuration in nanotubes? (ii) If not, why is this so, and for what single-walled nanotube diameter will the crossover occur as graphene can be considered infinite diameter tubes? (iii) How does the 555–777 divacancy influence its transport properties? *In situ* annealing studies of such defects in a dedicated environmental chamber under high-resolution conditions would be rewarding to study the effects of each symmetry-breaking mechanism. Combining tip-enhanced Raman and TEM studies on the same graphene defect could provide unique information about the dynamics of such defects and the changes in the different vibrational modes. A feasibility study using such defects is currently being carried out. However, it is a big challenge to make such defects. The possibility of tailoring the electronic properties of graphene using such defects has been investigated, although control over the precise location remains a challenge. Carbon adatoms can catalyze the formation and dissociation of bonds in graphene because of their under-coordination for bulk  $sp^2$  carbon atoms. Still, their exact role and observation of common compound defects in graphene remain unclear.

Most theoretical calculations based on first-principles DFT are limited to a few hundred atoms. At the same time, the accuracy and reliability of the calculation results are questionable when using empirical classical interatomic potentials with many atoms. Therefore, it would be desirable to have a fast

computational tool to calculate systems with complex defects and thousands of atoms. In this regard, tight-binding methods can bridge the gap between the first-principles DFT calculations and the simulations using empirical classical potentials. Moreover, the properties of the adatoms adsorbed on the graphene system are strongly dependent on the adsorption configuration (*e.g.*, isolated adatoms *versus* clusters), so it is crucial not only to understand these effects (configuration-dependent properties and migration) from a theoretical point of view but also to be able to probe them experimentally.

The doping of graphene with transition metals and their spintronics applications is underway. Thus, the study of magnetic substitutional impurities is essential for a theoretical understanding of magnetism for atomic defects in graphene and for explaining experiments in progress that dope graphene with elements of the traditional magnetic bulks (Fe, Co, and Ni). Besides, the origin of electrocatalytic activity and the nature of the electrochemical reaction processes on the  $M-N_x-G$  catalysts should be understood to open a new era for the design of graphene-based materials with superior catalytic activity toward electrochemical reactions. Such types of studies would motivate further research in this direction.

The line defect corresponding to grain boundaries in graphene should be paramount. It is well-known that the properties of polycrystalline materials are often dominated by the size of their grains and the atomic structure of the grain boundaries. Still, the role of such systems should be pronounced in graphene, where even a line defect can divide and disrupt a crystal. A more generalized means of forming various types of extended line defects (ELDs), for example, using foreign elements (doped ELDs), is quite demanding. Grain boundaries may govern the transport in such samples. The edges of graphene nanoribbons (GNRs) play a crucial role in modulating their electronic properties. Structural modification of the edges, such as bond reconstruction, edge functionalization, passivation, doping, and strain, leads to alteration of the  $\pi$ -network at the edges. These structural modifications are potential methods to tailor the geometries, stability, electronic properties, spin polarization, spin gap asymmetry, and size of the graphene bandgap. Maximizing the ultimate strength of defected graphene is necessary to optimize it into a versatile energy material. Therefore, a fundamental understanding of such defects' electronic and mechanical properties is essential. The linear defects corresponding to grain boundaries in graphene should be of prime importance because grain boundaries may govern the electronic transport in such samples because of their crucial role in 2D materials. Moreover, the characterization and understanding of the edge atomic structure and termination in graphene and multilayer graphene sheets are vital to future tailoring of the electronic and spin dynamics through controlled edge terminations. Information regarding the system of the intrinsic edges of graphene and multilayer graphene sheets produced *via* exfoliation is relatively unknown, and further work is needed to build an understanding.

Experimental measurements of the magnetic moment of defective graphene and traces of room temperature ferromagnetism are still limited. These difficulties in observing



ferromagnetism in graphene and graphene-based systems are poorly understood and remain debatable. In such conditions, theoretical studies predicting the defective graphene's magnetism using first-principles calculations are appreciable. Unfortunately, graphene's lack of intrinsic magnetism rules out its use for the spin-polarized current generation. One could use ferromagnetic electrodes as intermediates for spin injection, but the efficiency of such a setup is inadequate because of important contact-induced spin relaxation phenomena. Indeed, while AGNRs do not display magnetic ordering, edge-localized magnetic states have been predicted in ZGNRs. However, as these localized states are sensitive to edge roughness, their experimental observation has remained a real challenge for a long time. Although the formation energy of SW defects and the activation energy of SW transformations are reduced by several electron volts at the critical strain, such transformations are still kinetically limited. More significant strains should be applied to observe them experimentally. To heal vacancy defects in graphene in a controlled way would be appreciable. High-temperature thermal annealing, adding foreign atoms, or drawing support from some metal substrates can efficiently remove unwanted defects. However, it is still difficult to regulate the concentration of the defects in the actual experiments, especially for the large area of graphene or batch processing. Therefore, the nature of the healing mechanism should be explored.

Graphene and its derivatives have been used as a substrate for stem cells in regenerative medicine. To use stem cells in transplantation and tissue engineering, it is necessary to stimulate them properly and provide suitable synthetic or natural growth conditions. An additional benefit would be a scaffold material with a controllable and interactive interface with the living cells. Since carbon is an abundant and cheap element, its use for industrial applications would become a part of global sustainability planning by achieving it from CO<sub>2</sub> or waste CH<sub>4</sub>. As a result of their spectacular electronic, thermal, mechanical, and magnetic properties, graphene sheets are expected to offer an exceptional choice in electrochemical energy conversion and storage applications. However, fully realizing their applications in nanoelectronics, sensors, transparent electrodes, energy storage, conversion devices, and biomedicine still requires much fundamental research for the controlled introduction of intrinsic and extrinsic defects in the growth process in the future. This review is expected to understand the vital role of structural defects in graphene and consequently help investigate graphene defects for potential applications.

## Conflicts of interest

The authors declare no competing financial interest.

## Acknowledgements

Basic Science Research Program supported this work through the National Research Foundation of Korea funded by the Ministry of Education (NRF-2020R1A6A1A03043435).

## References

- 1 H. W. Kroto, J. R. Heath, S. C. O'Brien, R. F. Curl and R. E. Smalley, *Nature*, 1985, **318**, 162–163.
- 2 S. Iijima, *Nature*, 1991, **354**, 56–58.
- 3 K. S. Novoselov, A. K. Geim, S. V. Morozov, D.-e. Jiang, Y. Zhang, S. V. Dubonos, I. V. Grigorieva and A. A. Firsov, *Science*, 2004, **306**, 666–669.
- 4 P. R. Wallace, *Phys. Rev.*, 1947, **71**, 622.
- 5 A. K. Geim, *Phys. Scr.*, 2012, **2012**, 014003.
- 6 H.-P. Boehm, A. Clauss, G. Fischer and U. Hofmann, *Z. Anorg. Allg. Chem.*, 1962, **316**, 119–127.
- 7 R. Pearce, T. Iakimov, M. Andersson, L. Hultman, A. L. Spetz and R. Yakimova, *Sens. Actuators, B*, 2011, **155**, 451–455.
- 8 T. Kuila, S. Bose, P. Khanra, A. K. Mishra, N. H. Kim and J. H. Lee, *Biosens. Bioelectron.*, 2011, **26**, 4637–4648.
- 9 G. Singh, A. Choudhary, D. Haranath, A. G. Joshi, N. Singh, S. Singh and R. Pasricha, *Carbon*, 2012, **50**, 385–394.
- 10 F. Chen, J. Xia, D. K. Ferry and N. Tao, *Nano Lett.*, 2009, **9**, 2571–2574.
- 11 L.-F. Mao, *Nanotechnology*, 2009, **20**, 275203.
- 12 E. W. Hill, A. K. Geim, K. Novoselov, F. Schedin and P. Blake, *IEEE Trans. Magn.*, 2006, **42**, 2694–2696.
- 13 M. Kaukonen, A. Krasheninnikov, E. Kauppinen and R. Nieminen, *ACS Catal.*, 2013, **3**, 159–165.
- 14 Z. Qin, Z. Li, M. Zhang, B. Yang and R. Outlaw, *J. Power Sources*, 2012, **217**, 303–308.
- 15 G. Wang, B. Wang, X. Wang, J. Park, S. Dou, H. Ahn and K. Kim, *J. Mater. Chem.*, 2009, **19**, 8378–8384.
- 16 M. Pumera, *Energy Environ. Sci.*, 2011, **4**, 668–674.
- 17 Y. Niimi, T. Matsui, H. Kambara, K. Tagami, M. Tsukada and H. Fukuyama, *Appl. Surf. Sci.*, 2005, **241**, 43–48.
- 18 Y. Kobayashi, K.-i. Fukui, T. Enoki, K. Kusakabe and Y. Kaburagi, *Phys. Rev. B: Condens. Matter Mater. Phys.*, 2005, **71**, 193406.
- 19 D. Klein, *Chem. Phys. Lett.*, 1994, **217**, 261–265.
- 20 M. Fujita, K. Wakabayashi, K. Nakada and K. Kusakabe, *J. Phys. Soc. Jpn.*, 1996, **65**, 1920–1923.
- 21 R. Saito, M. Fujita, G. Dresselhaus and u. M. Dresselhaus, *Appl. Phys. Lett.*, 1992, **60**, 2204–2206.
- 22 Y.-W. Son, M. L. Cohen and S. G. Louie, *Phys. Rev. Lett.*, 2006, **97**, 216803.
- 23 L. Tapasztó, G. Dobrik, P. Lambin and L. P. Biro, *Nat. Nanotechnol.*, 2008, **3**, 397–401.
- 24 S. S. Datta, D. R. Strachan, S. M. Khamis and A. C. Johnson, *Nano Lett.*, 2008, **8**, 1912–1915.
- 25 C. Berger, Z. Song, X. Li, X. Wu, N. Brown, C. Naud, D. Mayou, T. Li, J. Hass and A. N. Marchenkov, *Science*, 2006, **312**, 1191–1196.
- 26 F. Banhart, J. Kotakoski and A. V. Krasheninnikov, *ACS Nano*, 2011, **5**, 26–41.
- 27 M. Maruyama, K. Kusakabe, S. Tsuneyuki, K. Akagi, Y. Yoshimoto and J. Yamauchi, *J. Phys. Chem. Solids*, 2004, **65**, 119–122.
- 28 D. Gunlycke, J. Li, J. Mintmire and C. White, *Appl. Phys. Lett.*, 2007, **91**, 112108.



- 29 O. Hod, V. Barone, J. E. Peralta and G. E. Scuseria, *Nano Lett.*, 2007, **7**, 2295–2299.
- 30 N. Gortjizadeh, A. A. Farajian, K. Esfarjani and Y. Kawazoe, *Phys. Rev. B: Condens. Matter Mater. Phys.*, 2008, **78**, 155427.
- 31 Q. Tang, Z. Zhou and Z. Chen, *Nanoscale*, 2013, **5**, 4541–4583.
- 32 M. N. Groves, C. Malardier-Jugroot and M. Jugroot, *J. Phys. Chem. C*, 2012, **116**, 10548–10556.
- 33 M. Groves, A. Chan, C. Malardier-Jugroot and M. Jugroot, *Chem. Phys. Lett.*, 2009, **481**, 214–219.
- 34 H. Liu, Y. Liu and D. Zhu, *J. Mater. Chem.*, 2011, **21**, 3335–3345.
- 35 Y.-H. Lu, M. Zhou, C. Zhang and Y.-P. Feng, *J. Phys. Chem. C*, 2009, **113**, 20156–20160.
- 36 E. Song, Z. Wen and Q. Jiang, *J. Phys. Chem. C*, 2011, **115**, 3678–3683.
- 37 Q. Jiang, Z. Ao, S. Li and Z. Wen, *RSC Adv.*, 2014, **4**, 20290–20296.
- 38 Y. Tang, Z. Yang and X. Dai, *Phys. Chem. Chem. Phys.*, 2012, **14**, 16566–16572.
- 39 T. Hongwei, F. Wei, W. Rui, L. Huiling and H. Xuri, *Mol. Phys.*, 2015, **113**, 3514–3523.
- 40 Y. Tang, Z. Yang and X. Dai, *J. Chem. Phys.*, 2011, **135**, 224704.
- 41 T. Alonso-Lanza, A. Ayuela and F. Aguilera-Granja, *Phys. Chem. Chem. Phys.*, 2016, **18**, 21913–21920.
- 42 A. Ambrosi, S. Y. Chee, B. Khezri, R. D. Webster, Z. Sofer and M. Pumera, *Angew. Chem., Int. Ed.*, 2012, **51**, 500–503.
- 43 M. D. Bhatt, G. Lee and J. S. Lee, *J. Phys. Chem. C*, 2016, **120**, 26435–26441.
- 44 W. Orellana, *J. Phys. Chem. C*, 2013, **117**, 9812–9818.
- 45 S. Gao, X. Wei, H. Liu, K. Geng, H. Wang, H. Moehwald and D. Shchukin, *J. Mater. Chem. A*, 2015, **3**, 23376–23384.
- 46 Z. Lu, G. Xu, C. He, T. Wang, L. Yang, Z. Yang and D. Ma, *Carbon*, 2015, **84**, 500–508.
- 47 A. Nazari, R. Faez and H. Shamloo, *Superlattices Microstruct.*, 2015, **86**, 483–492.
- 48 A. W. Robertson, B. Montanari, K. He, C. S. Allen, Y. A. Wu, N. M. Harrison, A. I. Kirkland and J. H. Warner, *ACS Nano*, 2013, **7**, 4495–4502.
- 49 O. V. Yazyev and L. Helm, *Phys. Rev. B: Condens. Matter Mater. Phys.*, 2007, **75**, 125408.
- 50 L. Rodrigo, P. Pou and R. Pérez, *Carbon*, 2016, **103**, 200–208.
- 51 Y. Ma, P. Lehtinen, A. S. Foster and R. M. Nieminen, *New J. Phys.*, 2004, **6**, 68.
- 52 F. Gao and S. Gao, *Sci. Rep.*, 2019, **9**, 1–5.
- 53 I. A. Pašti, A. Jovanović, A. S. Dobrota, S. V. Mentus, B. Johansson and N. V. Skorodumova, *Phys. Chem. Chem. Phys.*, 2018, **20**, 858–865.
- 54 A. Tapia, R. Peón-Escalante, C. Villanueva and F. Avilés, *Comput. Mater. Sci.*, 2012, **55**, 255–262.
- 55 A. Fedorov, Z. Popov, D. Fedorov, N. Eliseeva, M. Serjantova and A. Kuzubov, *Phys. Status Solidi B*, 2012, **249**, 2549–2552.
- 56 L. Liu, M. Qing, Y. Wang and S. Chen, *J. Mater. Sci. Technol.*, 2015, **31**, 599–606.
- 57 G.-D. Lee, C. Wang, E. Yoon, N.-M. Hwang, D.-Y. Kim and K. Ho, *Phys. Rev. Lett.*, 2005, **95**, 205501.
- 58 J. Kotakoski, A. Krasheninnikov, U. Kaiser and J. Meyer, *Phys. Rev. Lett.*, 2011, **106**, 105505.
- 59 S. T. Skowron, I. V. Lebedeva, A. M. Popov and E. Bichoutskaia, *Chem. Soc. Rev.*, 2015, **44**, 3143–3176.
- 60 W. Zhang, W.-C. Lu, H.-X. Zhang, K. Ho and C. Wang, *Carbon*, 2016, **110**, 330–335.
- 61 L. Wu, T. Hou, Y. Li, K. Chan and S.-T. Lee, *J. Phys. Chem. C*, 2013, **117**, 17066–17072.
- 62 S. N. Shirodkar and U. V. Waghmare, *Phys. Rev. B: Condens. Matter Mater. Phys.*, 2012, **86**, 165401.
- 63 J. Ma, D. Alfè, A. Michaelides and E. Wang, *Phys. Rev. B: Condens. Matter Mater. Phys.*, 2009, **80**, 033407.
- 64 L. Li, S. Reich and J. Robertson, *Phys. Rev. B: Condens. Matter Mater. Phys.*, 2005, **72**, 184109.
- 65 X. Dai, J. Zhao, M. Xie, Y. Tang, Y. Li and B. Zhao, *Eur. Phys. J. B*, 2011, **80**, 343–349.
- 66 R. Dettori, E. Cadelano and L. Colombo, *J. Phys.: Condens. Matter*, 2012, **24**, 104020.
- 67 H. Yin, X. Shi, C. He, M. Martinez-Canales, J. Li, C. J. Pickard, C. Tang, T. Ouyang, C. Zhang and J. Zhong, *Phys. Rev. B*, 2019, **99**, 041405.
- 68 D. J. Appelhans, Z. Lin and M. T. Lusk, *Phys. Rev. B: Condens. Matter Mater. Phys.*, 2010, **82**, 073410.
- 69 J. Lahiri, Y. Lin, P. Bozkurt, I. I. Oleynik and M. Batzill, *Nat. Nanotechnol.*, 2010, **5**, 326–329.
- 70 O. V. Yazyev, *Rep. Prog. Phys.*, 2010, **73**, 056501.
- 71 R. Ansari, S. Ajori and B. Motevalli, *Superlattices Microstruct.*, 2012, **51**, 274–289.
- 72 A. Zandiatashbar, G.-H. Lee, S. J. An, S. Lee, N. Mathew, M. Terrones, T. Hayashi, C. R. Picu, J. Hone and N. Koratkar, *Nat. Commun.*, 2014, **5**, 1–9.
- 73 G. López-Polín, C. Gómez-Navarro, V. Parente, F. Guinea, M. I. Katsnelson, F. Perez-Murano and J. Gómez-Herrero, *Nat. Phys.*, 2015, **11**, 26–31.
- 74 Y. Li, Z. Zhou, G. Yu, W. Chen and Z. Chen, *J. Phys. Chem. C*, 2010, **114**, 6250–6254.
- 75 Y. Kim, J. Ihm, E. Yoon and G.-D. Lee, *Phys. Rev. B: Condens. Matter Mater. Phys.*, 2011, **84**, 075445.
- 76 Q.-K. Li, X.-F. Li, G. Zhang and J. Jiang, *J. Am. Chem. Soc.*, 2018, **140**, 15149–15152.
- 77 M. Lalitha, S. S. Mahadevan and S. Lakshmi pathi, *J. Mater. Sci.*, 2017, **52**, 815–831.
- 78 Y. Tang, Z. Yang, X. Dai, D. Ma and Z. Fu, *J. Phys. Chem. C*, 2013, **117**, 5258–5268.
- 79 F. Li, J. Zhao and Z. Chen, *J. Phys. Chem. C*, 2012, **116**, 2507–2514.
- 80 H.-p. Zhang, X.-g. Luo, H.-t. Song, X.-y. Lin, X. Lu and Y. Tang, *Appl. Surf. Sci.*, 2014, **317**, 511–516.
- 81 P. Wu, P. Du, H. Zhang and C. Cai, *Phys. Chem. Chem. Phys.*, 2015, **17**, 1441–1449.
- 82 Y. Tang, W. Chen, Z. Shen, C. Li, D. Ma and X. Dai, *Phys. Chem. Chem. Phys.*, 2018, **20**, 2284–2295.
- 83 M. Saito, K. Yamashita and T. Oda, *Jpn. J. Appl. Phys.*, 2007, **46**, L1185.
- 84 A. El-Barbary, R. Telling, C. Ewels, M. Heggie and P. Briddon, *Phys. Rev. B: Condens. Matter Mater. Phys.*, 2003, **68**, 144107.



- 85 P. O. Lehtinen, A. S. Foster, Y. Ma, A. Krasheninnikov and R. M. Nieminen, *Phys. Rev. Lett.*, 2004, **93**, 187202.
- 86 J. M. Carlsson and M. Scheffler, *Phys. Rev. Lett.*, 2006, **96**, 046806.
- 87 R. G. Amorim, A. Fazzio, A. Antonelli, F. D. Novaes and A. J. da Silva, *Nano Lett.*, 2007, **7**, 2459–2462.
- 88 M. M. Ugeda, I. Brihuega, F. Guinea and J. M. Gómez-Rodríguez, *Phys. Rev. Lett.*, 2010, **104**, 096804.
- 89 J. Palacios and F. Ynduráin, *Phys. Rev. B: Condens. Matter Mater. Phys.*, 2012, **85**, 245443.
- 90 H. Padmanabhan and B. Nanda, *Phys. Rev. B*, 2016, **93**, 165403.
- 91 Y. Zhang, F. Gao, S. Gao and L. He, *Sci. Bull.*, 2020, **65**, 194–200.
- 92 M. G. Menezes and R. B. Capaz, *J. Phys.: Condens. Matter*, 2015, **27**, 335302.
- 93 Y. Zhou, A. Lii-Rosales, M. Kim, M. Wallingford, D. Jing, M. C. Tringides, C.-Z. Wang and P. A. Thiel, *Carbon*, 2018, **127**, 305–311.
- 94 M. Buettner, P. Choudhury, J. K. Johnson and J. T. Yates Jr, *Carbon*, 2011, **49**, 3937–3952.
- 95 T. Hu, D. Ma, Q. Fang, P. Zhang, X. Liu, R. Wei, Y. Pan, K. Xu and F. Ma, *Carbon*, 2019, **146**, 313–319.
- 96 Z. Yang, S. Bhowmick, F. G. Sen, A. Banerji and A. T. Alpas, *Sci. Rep.*, 2018, **8**, 1–13.
- 97 X.-L. Ye, J. Cai, X.-D. Yang, X.-Y. Tang, Z.-Y. Zhou, Y.-Z. Tan, S.-Y. Xie and L.-S. Zheng, *J. Mater. Chem. A*, 2017, **5**, 24257–24262.
- 98 P. A. Denis and F. Iribarne, *J. Phys. Chem. C*, 2013, **117**, 19048–19055.
- 99 X. Peng and R. Ahuja, *Nano Lett.*, 2008, **8**, 4464–4468.
- 100 M. G. Menezes, R. B. Capaz and J. L. Faria, *Phys. Rev. B: Condens. Matter Mater. Phys.*, 2010, **82**, 245414.
- 101 Y. Orimoto, K. Otsuka, K. Yagyu, H. Tochiwara, T. Suzuki and Y. Aoki, *J. Phys. Chem. C*, 2017, **121**, 7294–7302.
- 102 F. Yao, F. Gunes, H. Q. Ta, S. M. Lee, S. J. Chae, K. Y. Sheem, C. S. Cojocar, S. S. Xie and Y. H. Lee, *J. Am. Chem. Soc.*, 2012, **134**, 8646–8654.
- 103 A. Markevich, R. Jones, S. Öberg, M. Rayson, J. Goss and P. Briddon, *Phys. Rev. B: Condens. Matter Mater. Phys.*, 2012, **86**, 045453.
- 104 T. P. Kaloni, M. U. Kahaly, Y. Cheng and U. Schwingenschlögl, *J. Mater. Chem.*, 2012, **22**, 23340–23343.
- 105 J. Coraux, A. T. N 'Diaye, C. Busse and T. Michely, *Nano Lett.*, 2008, **8**, 565–570.
- 106 J. Červenka, M. Katsnelson and C. Flipse, *Nat. Phys.*, 2009, **5**, 840–844.
- 107 O. V. Yazyev and S. G. Louie, *Nat. Mater.*, 2010, **9**, 806–809.
- 108 B. W. Jeong, J. Ihm and G.-D. Lee, *Phys. Rev. B: Condens. Matter Mater. Phys.*, 2008, **78**, 165403.
- 109 L. Kou, C. Tang, W. Guo and C. Chen, *ACS Nano*, 2011, **5**, 1012–1017.
- 110 X. Lin and J. Ni, *Phys. Rev. B: Condens. Matter Mater. Phys.*, 2011, **84**, 075461.
- 111 A. Hashimoto, K. Suenaga, A. Gloter, K. Urita and S. Iijima, *Nature*, 2004, **430**, 870–873.
- 112 M. H. Gass, U. Bangert, A. L. Bleloch, P. Wang, R. R. Nair and A. Geim, *Nat. Nanotechnol.*, 2008, **3**, 676–681.
- 113 J. C. Meyer, C. Kisielowski, R. Erni, M. D. Rossell, M. Crommie and A. Zettl, *Nano Lett.*, 2008, **8**, 3582–3586.
- 114 J. H. Warner, M. H. Rummeli, L. Ge, T. Gemming, B. Montanari, N. M. Harrison, B. Büchner and G. A. D. Briggs, *Nat. Nanotechnol.*, 2009, **4**, 500–504.
- 115 Ç. O. Girit, J. C. Meyer, R. Erni, M. D. Rossell, C. Kisielowski, L. Yang, C.-H. Park, M. Crommie, M. L. Cohen and S. G. Louie, *Science*, 2009, **323**, 1705–1708.
- 116 L. Tapasztó, G. Dobrik, P. Nemes-Incze, G. Vertesy, P. Lambin and L. P. Biro, *Phys. Rev. B: Condens. Matter Mater. Phys.*, 2008, **78**, 233407.
- 117 T. Susi, M. Kaukonen, P. Havu, M. P. Ljungberg, P. Ayala and E. I. Kauppinen, *Beilstein J. Nanotechnol.*, 2014, **5**, 121–132.
- 118 L. Openov and A. Podlivaev, *Phys. Solid State*, 2015, **57**, 1477–1481.
- 119 H. F. Bettinger, B. I. Yakobson and G. E. Scuseria, *J. Am. Chem. Soc.*, 2003, **125**, 5572–5580.
- 120 V. H. Crespi, L. X. Benedict, M. L. Cohen and S. G. Louie, *Phys. Rev. B: Condens. Matter Mater. Phys.*, 1996, **53**, R13303.
- 121 M. B. Nardelli, B. I. Yakobson and J. Bernholc, *Phys. Rev. B: Condens. Matter Mater. Phys.*, 1998, **57**, R4277.
- 122 C. Ewels, M. Heggge and P. Briddon, *Chem. Phys. Lett.*, 2002, **351**, 178–182.
- 123 W.-W. Wang, J.-S. Dang, J.-J. Zheng, X. Zhao, E. Ōsawa and S. Nagase, *J. Mater. Chem.*, 2012, **22**, 16370–16375.
- 124 C. Wang and Y.-h. Ding, *J. Mater. Chem. A*, 2013, **1**, 1885–1891.
- 125 L. Chen, H. Hu, Y. Ouyang, H. Pan, Y. Sun and F. Liu, *Carbon*, 2011, **49**, 3356–3361.
- 126 L. Chen, J. Li, D. Li, M. Wei and X. Wang, *Solid State Commun.*, 2012, **152**, 1985–1989.
- 127 Y. An, A. F. Oliveira, T. Brumme, A. Kuc and T. Heine, *Adv. Mater.*, 2020, **32**, 2002442.
- 128 J. Kumar, Ansh and M. Shrivastava, *ACS Omega*, 2020, **5**, 31281–31288.
- 129 E. Zaminpayma, M. E. Razavi and P. Nayebi, *Appl. Surf. Sci.*, 2017, **414**, 101–106.
- 130 H. Wang, Y. Wang, B. Bai, X. Guo and J. Xue, *Appl. Surf. Sci.*, 2020, **531**, 147347.
- 131 X. Long, F. Zhao, H. Liu, J. Huang, Y. Lin, J. Zhu and S. Luo, *J. Phys. Chem. C*, 2015, **119**, 7453–7460.
- 132 S. Ebrahimi and M. Azizi, *Mol. Simul.*, 2018, **44**, 236–242.
- 133 D. Boukhvalov and M. Katsnelson, *Nano Lett.*, 2008, **8**, 4373–4379.
- 134 B. Mortazavi and S. Ahzi, *Carbon*, 2013, **63**, 460–470.
- 135 S. Yadav, Z. Zhu and C. V. Singh, *Int. J. Hydrogen Energy*, 2014, **39**, 4981–4995.
- 136 E. J. Duplock, M. Scheffler and P. J. Lindan, *Phys. Rev. Lett.*, 2004, **92**, 225502.
- 137 D. Datta, J. Li, N. Koratkar and V. B. Shenoy, *Carbon*, 2014, **80**, 305–310.
- 138 D. Datta, J. Li and V. B. Shenoy, *ACS Appl. Mater. Interfaces*, 2014, **6**, 1788–1795.



- 139 Y. Zhang, S.-Y. Li, H. Huang, W.-T. Li, J.-B. Qiao, W.-X. Wang, L.-J. Yin, K.-K. Bai, W. Duan and L. He, *Phys. Rev. Lett.*, 2016, **117**, 166801.
- 140 H. Amara, S. Latil, V. Meunier, P. Lambin and J.-C. Charlier, *Phys. Rev. B: Condens. Matter Mater. Phys.*, 2007, **76**, 115423.
- 141 A. Krasheninnikov, P. Lehtinen, A. Foster and R. Nieminen, *Chem. Phys. Lett.*, 2006, **418**, 132–136.
- 142 D. Midtvedt and A. Croy, *J. Phys.: Condens. Matter*, 2016, **28**, 045302.
- 143 M. Sepioni, R. Nair, S. Rablen, J. Narayanan, F. Tuna, R. Winpenny, A. Geim and I. Grigorieva, *Phys. Rev. Lett.*, 2010, **105**, 207205.
- 144 Y. Wang, Y. Huang, Y. Song, X. Zhang, Y. Ma, J. Liang and Y. Chen, *Nano Lett.*, 2009, **9**, 220–224.
- 145 M. Sepioni, R. Nair, I.-L. Tsai, A. Geim and I. Grigorieva, *Europhys. Lett.*, 2012, **97**, 47001.
- 146 Z. Yue, D. Seo, K. Ostrikov and X. Wang, *Appl. Phys. Lett.*, 2014, **104**, 092417.
- 147 A. M. Valencia and M. J. Caldas, *Phys. Rev. B*, 2017, **96**, 125431.
- 148 S. Y. Kim and H. S. Park, *Nanotechnology*, 2010, **21**, 105710.
- 149 C. Reddy, S. Rajendran and K. Liew, *Int. J. Nanosci.*, 2005, **4**, 631–636.
- 150 M. Wang, C. Yan, L. Ma, N. Hu and M. Chen, *Comput. Mater. Sci.*, 2012, **54**, 236–239.
- 151 C. Carpenter, A. Ramasubramaniam and D. Maroudas, *Appl. Phys. Lett.*, 2012, **100**, 203105.
- 152 C. Carpenter, D. Maroudas and A. Ramasubramaniam, *Appl. Phys. Lett.*, 2013, **103**, 013102.
- 153 X. Sun, Z. Fu, M. Xia and Y. Xu, *Theor. App. Mech. Lett.*, 2014, **4**, 051002.
- 154 M. Katsnelson and A. Geim, *Philos. Trans. Royal Soc. A*, 2008, **366**, 195–204.
- 155 A. J. Stone and D. J. Wales, *Chem. Phys. Lett.*, 1986, **128**, 501–503.
- 156 A. Fedorov, D. Fedorov, Z. Popov, Y. E. Anan'eva, N. Eliseeva and A. Kuzubov, *J. Exp. Theor. Phys.*, 2011, **112**, 820–824.
- 157 W. Zhang, W.-C. Lu, H.-X. Zhang, K. Ho and C. Wang, *J. Phys.: Condens. Matter*, 2016, **28**, 115001.
- 158 M. M. Ugeda, I. Brihuega, F. Hiebel, P. Mallet, J.-Y. Veuillen, J. M. Gómez-Rodríguez and F. Ynduráin, *Phys. Rev. B: Condens. Matter Mater. Phys.*, 2012, **85**, 121402.
- 159 Z. Hou and K. Terakura, *J. Phys. Chem. C*, 2015, **119**, 4922–4933.
- 160 X. Gao, L. Liu, S. Irlé and S. Nagase, *Angew. Chem., Int. Ed.*, 2010, **49**, 3200–3202.
- 161 P. Hirunsit, M. Liangruksa and P. Khanchaitit, *Carbon*, 2016, **108**, 7–20.
- 162 A. Lu and B. Pan, *Phys. Rev. Lett.*, 2004, **92**, 105504.
- 163 J. Kotakoski, A. Krasheninnikov and K. Nordlund, *Phys. Rev. B: Condens. Matter Mater. Phys.*, 2006, **74**, 245420.
- 164 L. Liu, J. Gao, X. Zhang, T. Yan and F. Ding, *Nanoscale*, 2014, **6**, 5729–5734.
- 165 W. S. Paz, W. L. Scopel and J. C. Freitas, *Solid State Commun.*, 2013, **175**, 71–75.
- 166 E. Santos, S. Riikonen, D. Sánchez-Portal and A. Ayuela, *J. Phys. Chem. C*, 2012, **116**, 7602–7606.
- 167 O. Cretu, A. V. Krasheninnikov, J. A. Rodríguez-Manzo, L. Sun, R. M. Nieminen and F. Banhart, *Phys. Rev. Lett.*, 2010, **105**, 196102.
- 168 J. Kotakoski, J. C. Meyer, S. Kurasch, D. Santos-Cottin, U. Kaiser and A. V. Krasheninnikov, *Phys. Rev. B: Condens. Matter Mater. Phys.*, 2011, **83**, 245420.
- 169 B. Wang, Y. Puzyrev and S. T. Pantelides, *Carbon*, 2011, **49**, 3983–3988.
- 170 J. Kotakoski, D. Santos-Cottin and A. V. Krasheninnikov, *ACS Nano*, 2012, **6**, 671–676.
- 171 J. Lu, Y. Bao, C. L. Su and K. P. Loh, *ACS Nano*, 2013, **7**, 8350–8357.
- 172 A. R. Botello-Méndez, X. Declerck, M. Terrones, H. Terrones and J.-C. Charlier, *Nanoscale*, 2011, **3**, 2868–2872.
- 173 H. Huang, Y. Xu, X. Zou, J. Wu and W. Duan, *Phys. Rev. B: Condens. Matter Mater. Phys.*, 2013, **87**, 205415.
- 174 Y. H. Lee, S. G. Kim and D. Tománek, *Phys. Rev. Lett.*, 1997, **78**, 2393.
- 175 P. O. Lehtinen, A. S. Foster, A. Ayuela, A. Krasheninnikov, K. Nordlund and R. M. Nieminen, *Phys. Rev. Lett.*, 2003, **91**, 017202.
- 176 L. Tsetseris and S. T. Pantelides, *Carbon*, 2009, **47**, 901–908.
- 177 A. W. Robertson, G.-D. Lee, K. He, E. Yoon, A. I. Kirkland and J. H. Warner, *Nano Lett.*, 2014, **14**, 3972–3980.
- 178 J. C. Meyer, C. O. Girit, M. Crommie and A. Zettl, *Nature*, 2008, **454**, 319–322.
- 179 G.-D. Lee, A. W. Robertson, S. Lee, Y.-C. Lin, J.-W. Oh, H. Park, Y.-C. Joo, E. Yoon, K. Suenaga and J. H. Warner, *Sci. Adv.*, 2020, **6**, eaba4942.
- 180 C. Ataca, E. Aktürk, H. Şahin and S. Ciraci, *J. Appl. Phys.*, 2011, **109**, 013704.
- 181 W.-C. Lu, C. Wang, L.-Z. Zhao, W. Qin and K. Ho, *Phys. Rev. B: Condens. Matter Mater. Phys.*, 2015, **92**, 035206.
- 182 R. V. Siriwardane, M.-S. Shen, E. P. Fisher and J. A. Poston, *Energy Fuels*, 2001, **15**, 279–284.
- 183 Z. Chen, S. Deng, H. Wei, B. Wang, J. Huang and G. Yu, *Front. Environ. Sci. Eng.*, 2013, **7**, 326–340.
- 184 H. Jüntgen, *Fuel*, 1986, **65**, 1436–1446.
- 185 M. Sevilla and R. Mokaya, *Energy Environ. Sci.*, 2014, **7**, 1250–1280.
- 186 A. D. Roberts, X. Li and H. Zhang, *Chem. Soc. Rev.*, 2014, **43**, 4341–4356.
- 187 F. Banhart, *Nanoscale*, 2009, **1**, 201–213.
- 188 Y. Gan, L. Sun and F. Banhart, *Small*, 2008, **4**, 587–591.
- 189 J. A. Rodríguez-Manzo, O. Cretu and F. Banhart, *ACS Nano*, 2010, **4**, 3422–3428.
- 190 A. Krasheninnikov, P. Lehtinen, A. S. Foster, P. Pyykkö and R. M. Nieminen, *Phys. Rev. Lett.*, 2009, **102**, 126807.
- 191 Y. Mao, J. Yuan and J. Zhong, *J. Phys.: Condens. Matter*, 2008, **20**, 115209.
- 192 H. Sevinçli, M. Topsakal, E. Durgun and S. Ciraci, *Phys. Rev. B: Condens. Matter Mater. Phys.*, 2008, **77**, 195434.
- 193 J. Hu, J. Alicea, R. Wu and M. Franz, *Phys. Rev. Lett.*, 2012, **109**, 266801.
- 194 I. Shteplyuk, N. M. Caffrey, T. Iakimov, V. Khranovskyy, I. A. Abrikosov and R. Yakimova, *Sci. Rep.*, 2017, **7**, 1–17.



- 195 N. Dimakis, F. A. Flor, A. Salgado, K. Adjibi, S. Vargas and J. Saenz, *Appl. Surf. Sci.*, 2017, **421**, 252–259.
- 196 H. Salehi, M. Moaddeli and P. Amiri, *Surf. Sci.*, 2016, **647**, 96–102.
- 197 Y. Tang, Z. Yang and X. Dai, *J. Magn. Magn. Mater.*, 2011, **323**, 2441–2447.
- 198 Z. Guan, S. Ni and S. Hu, *ACS Omega*, 2020, **5**, 5900–5910.
- 199 N. T. T. Tran, D. K. Nguyen, S. Y. Lin, G. Gumbs and M. F. Lin, *ChemPhysChem*, 2019, **20**, 2473–2481.
- 200 B. A. Barker, A. J. Bradley, M. M. Ugeda, S. Coh, A. Zettl, M. F. Crommie, S. G. Louie and M. L. Cohen, *Phys. Rev. B*, 2019, **99**, 075431.
- 201 B. P. Paudel, N. Pantha and N. P. Adhikari, *Journal of Nepal Physical Society*, 2015, **3**, 24–34.
- 202 N. Pantha, S. Thapa and N. P. Adhikari, *Journal of Institute of Science and Technology*, 2020, **25**, 15–23.
- 203 L. Liu, Z. Zhou, Q. Guo, Z. Yan, Y. Yao and D. W. Goodman, *Surf. Sci.*, 2011, **605**, L47–L50.
- 204 R. Thapa, D. Sen, M. Mitra and K. Chattopadhyay, *Phys. B*, 2011, **406**, 368–373.
- 205 A. Fenta, C. Amorim, J. Gonçalves, N. Fortunato, M. Barbosa, J. Araujo, M. Houssa, S. Cottenier, M. Van Bael and J. Correia, *J. Phys.: Mater.*, 2020, **4**, 015002.
- 206 M. Manadé, F. Viñes and F. Illas, *Carbon*, 2015, **95**, 525–534.
- 207 M. Legesse, F. El Mellouhi, E. T. Bentría, M. E. Madjet, T. S. Fisher, S. Kais and F. H. Alharbi, *Appl. Surf. Sci.*, 2017, **394**, 98–107.
- 208 N. Yang, D. Yang, L. Chen, D. Liu, M. Cai and X. Fan, *Nanoscale Res. Lett.*, 2017, **12**, 1–7.
- 209 A. Urich, A. Pospischil, M. M. Furchi, D. Dietze, K. Unterrainer and T. Mueller, *Appl. Phys. Lett.*, 2012, **101**, 153113.
- 210 Q. M. Ramasse, R. Zan, U. Bangert, D. W. Boukhvalov, Y.-W. Son and K. S. Novoselov, *ACS Nano*, 2012, **6**, 4063–4071.
- 211 J. Lee, K. S. Novoselov and H. S. Shin, *ACS Nano*, 2011, **5**, 608–612.
- 212 S. Sarkar, M. L. Moser, X. Tian, X. Zhang, Y. F. Al-Hadeethi and R. C. Haddon, *Chem. Mater.*, 2014, **26**, 184–195.
- 213 R. Zan, U. Bangert, Q. Ramasse and K. S. Novoselov, *Nano Lett.*, 2011, **11**, 1087–1092.
- 214 H. Wang, K. Li, Y. Cheng, Q. Wang, Y. Yao, U. Schwingenschlögl, X. Zhang and W. Yang, *Nanoscale*, 2012, **4**, 2920–2925.
- 215 F. Schedin, E. Lidorikis, A. Lombardo, V. G. Kravets, A. K. Geim, A. N. Grigorenko, K. S. Novoselov and A. C. Ferrari, *ACS Nano*, 2010, **4**, 5617–5626.
- 216 P. Wang, D. Zhang, L. Zhang and Y. Fang, *Chem. Phys. Lett.*, 2013, **556**, 146–150.
- 217 W.-H. Park, M. Jung, J.-S. Moon, S. Hwan Noh, T. Hyeong Kim, M. Ho Joo and K. Ho Park, *Appl. Phys. Lett.*, 2013, **103**, 071903.
- 218 H. Kim, I. Song, C. Park, M. Son, M. Hong, Y. Kim, J. S. Kim, H.-J. Shin, J. Baik and H. C. Choi, *ACS Nano*, 2013, **7**, 6575–6582.
- 219 H.-C. Lin, Y.-Z. Chen, Y.-C. Wang and Y.-L. Chueh, *J. Phys. Chem. C*, 2015, **119**, 6835–6842.
- 220 H. C. Lee, H. Bong, M. S. Yoo, M. Jo and K. Cho, *Small*, 2018, **14**, 1801181.
- 221 P. Rani and V. Jindal, *RSC Adv.*, 2013, **3**, 802–812.
- 222 C. Wang, K. Schouteden, Q.-H. Wu, Z. Li, J. Jiang and C. Van Haesendonck, *Nanotechnology*, 2016, **27**, 365702.
- 223 H.-P. Komsa, J. Kotakoski, S. Kurasch, O. Lehtinen, U. Kaiser and A. V. Krasheninnikov, *Phys. Rev. Lett.*, 2012, **109**, 035503.
- 224 Z.-H. Sheng, H.-L. Gao, W.-J. Bao, F.-B. Wang and X.-H. Xia, *J. Mater. Chem.*, 2012, **22**, 390–395.
- 225 S. Wang, L. Zhang, Z. Xia, A. Roy, D. W. Chang, J. B. Baek and L. Dai, *Angew. Chem., Int. Ed.*, 2012, **51**, 4209–4212.
- 226 L. Zhang and Z. Xia, *J. Phys. Chem. C*, 2011, **115**, 11170–11176.
- 227 L. Zhang, J. Niu, L. Dai and Z. Xia, *Langmuir*, 2012, **28**, 7542–7550.
- 228 S. Yang, L. Zhi, K. Tang, X. Feng, J. Maier and K. Müllen, *Adv. Funct. Mater.*, 2012, **22**, 3634–3640.
- 229 I. Y. Jeon, S. Zhang, L. Zhang, H. J. Choi, J. M. Seo, Z. Xia, L. Dai and J. B. Baek, *Adv. Mater.*, 2013, **25**, 6138–6145.
- 230 L. Zhang, J. Niu, M. Li and Z. Xia, *J. Phys. Chem. C*, 2014, **118**, 3545–3553.
- 231 R. A. Sidik, A. B. Anderson, N. P. Subramanian, S. P. Kumaraguru and B. N. Popov, *J. Phys. Chem. B*, 2006, **110**, 1787–1793.
- 232 E. Vayner and A. B. Anderson, *J. Phys. Chem. C*, 2007, **111**, 9330–9336.
- 233 L. Yu, X. Pan, X. Cao, P. Hu and X. Bao, *J. Catal.*, 2011, **282**, 183–190.
- 234 R. Lv, Q. Li, A. R. Botello-Méndez, T. Hayashi, B. Wang, A. Berkdemir, Q. Hao, A. L. Elías, R. Cruz-Silva and H. R. Gutiérrez, *Sci. Rep.*, 2012, **2**, 1–8.
- 235 Y. Yamada, J. Kim, S. Matsuo and S. Sato, *Carbon*, 2014, **70**, 59–74.
- 236 Y. Yamada, H. Tanaka, S. Kubo and S. Sato, *Carbon*, 2021, **185**, 342–367.
- 237 Y. Yamada, H. Yasuda, K. Murota, M. Nakamura, T. Sodesawa and S. Sato, *J. Mater. Sci.*, 2013, **48**, 8171–8198.
- 238 R. Chen, H. Li, D. Chu and G. Wang, *J. Phys. Chem. C*, 2009, **113**, 20689–20697.
- 239 K. A. Kurak and A. B. Anderson, *J. Phys. Chem. C*, 2009, **113**, 6730–6734.
- 240 D. Guo, R. Shibuya, C. Akiba, S. Saji, T. Kondo and J. Nakamura, *Science*, 2016, **351**, 361–365.
- 241 K. Takeyasu, M. Furukawa, Y. Shimoyama, S. K. Singh and J. Nakamura, *Angew. Chem., Int. Ed.*, 2021, **60**, 5121–5124.
- 242 T. Ishii, M. Philavanh, J. Negishi, E. Inukai and J.-i. Ozaki, *ACS Catal.*, 2022, **12**, 1288–1297.
- 243 S.-F. Huang, K. Terakura, T. Ozaki, T. Ikeda, M. Boero, M. Oshima, J.-i. Ozaki and S. Miyata, *Phys. Rev. B: Condens. Matter Mater. Phys.*, 2009, **80**, 235410.
- 244 L. Zhao, R. He, K. T. Rim, T. Schiros, K. S. Kim, H. Zhou, C. Gutiérrez, S. Chockalingam, C. J. Arguello and L. Pálková, *Science*, 2011, **333**, 999–1003.
- 245 T. Marangoni, D. Haberer, D. J. Rizzo, R. R. Cloke and F. R. Fischer, *Chem.–Eur. J.*, 2016, **22**, 13037–13040.



- 246 F. Banhart, J.-C. Charlier and P. Ajayan, *Phys. Rev. Lett.*, 2000, **84**, 686.
- 247 M. Ushiro, K. Uno, T. Fujikawa, Y. Sato, K. Tohji, F. Watari, W.-J. Chun, Y. Koike and K. Asakura, *Phys. Rev. B: Condens. Matter Mater. Phys.*, 2006, **73**, 144103.
- 248 M. D. Bhatt and G. Kim, *Appl. Surf. Sci.*, 2021, **569**, 150999.
- 249 N. Zhou, N. Wang, Z. Wu and L. Li, *Catalysts*, 2018, **8**, 509.
- 250 Y. Yamada, K. Murota, R. Fujita, J. Kim, A. Watanabe, M. Nakamura, S. Sato, K. Hata, P. Ercius and J. Ciston, *J. Am. Chem. Soc.*, 2014, **136**, 2232–2235.
- 251 J. A. Rodriguez-Manzo and F. Banhart, *Nano Lett.*, 2009, **9**, 2285–2289.
- 252 W. Zhou, M. D. Kapetanakis, M. P. Prange, S. T. Pantelides, S. J. Pennycook and J.-C. Idrobo, *Phys. Rev. Lett.*, 2012, **109**, 206803.
- 253 W. Zhou, J. Lee, J. Nanda, S. T. Pantelides, S. J. Pennycook and J.-C. Idrobo, *Nat. Nanotechnol.*, 2012, **7**, 161–165.
- 254 F. Bonaccorso, Z. Sun, T. Hasan and A. Ferrari, *Nat. Photonics*, 2010, **4**, 611–622.
- 255 A. Lopez-Bezanilla, W. Zhou and J.-C. Idrobo, *J. Phys. Chem. Lett.*, 2014, **5**, 1711–1718.
- 256 C.-p. Cheng, H.-f. Hu, Z.-j. Zhang, Q. Liu, Y. Chen and P. Peng, *Mod. Phys. Lett. B*, 2014, **28**, 1450229.
- 257 M. M. Ervasti, Z. Fan, A. Uppstu, A. V. Krashenninnikov and A. Harju, *Phys. Rev. B: Condens. Matter Mater. Phys.*, 2015, **92**, 235412.
- 258 E. J. Santos, A. Ayuela and D. Sánchez-Portal, *New J. Phys.*, 2010, **12**, 053012.
- 259 J. Maruyama, N. Fukui, M. Kawaguchi and I. Abe, *J. Power Sources*, 2008, **182**, 489–495.
- 260 V. Bambagioni, C. Bianchini, J. Filippi, A. Lavacchi, W. Oberhauser, A. Marchionni, S. Moneti, F. Vizza, R. Psaro and V. Dal Santo, *J. Power Sources*, 2011, **196**, 2519–2529.
- 261 Q. He, X. Yang, R. He, A. Bueno-López, H. Miller, X. Ren, W. Yang and B. E. Koel, *J. Power Sources*, 2012, **213**, 169–179.
- 262 R. Yang, K. Stevens and J. Dahn, *J. Electrochem. Soc.*, 2007, **155**, B79.
- 263 Z. Zhang, S. Yang, M. Dou, H. Liu, L. Gu and F. Wang, *RSC Adv.*, 2016, **6**, 67049–67056.
- 264 M. D. Bhatt, G. Lee and J. S. Lee, *Electrochim. Acta*, 2017, **228**, 619–627.
- 265 Y. Li, R. Hu, X. Wan, J. X. Shang, F. H. Wang and J. Shui, *Adv. Theory Simul.*, 2020, **3**, 2000054.
- 266 D. Li, Y. Jia, G. Chang, J. Chen, H. Liu, J. Wang, Y. Hu, Y. Xia, D. Yang and X. Yao, *Chem*, 2018, **4**, 2345–2356.
- 267 N. Zhang, B. Zhou, D. Li, D. Qi, Y. Wu, H. Zheng and B. Yang, *Nanomaterials*, 2022, **12**, 1044.
- 268 S. Malola, H. Häkkinen and P. Koskinen, *Phys. Rev. B: Condens. Matter Mater. Phys.*, 2010, **81**, 165447.
- 269 P. Y. Huang, C. S. Ruiz-Vargas, A. M. Van Der Zande, W. S. Whitney, M. P. Levendorf, J. W. Kevek, S. Garg, J. S. Alden, C. J. Hustedt and Y. Zhu, *Nature*, 2011, **469**, 389–392.
- 270 S. Chen, Q. Wu, C. Mishra, J. Kang, H. Zhang, K. Cho, W. Cai, A. A. Balandin and R. S. Ruoff, *Nat. Mater.*, 2012, **11**, 203–207.
- 271 Z. G. Fthenakis and D. Tománek, *Phys. Rev. B: Condens. Matter Mater. Phys.*, 2012, **86**, 125418.
- 272 F. Hao, D. Fang and Z. Xu, *Appl. Phys. Lett.*, 2011, **99**, 041901.
- 273 A. Bagri, S.-P. Kim, R. S. Ruoff and V. B. Shenoy, *Nano Lett.*, 2011, **11**, 3917–3921.
- 274 Y. Lu and J. Guo, *Appl. Phys. Lett.*, 2012, **101**, 043112.
- 275 A. Y. Serov, Z.-Y. Ong and E. Pop, *Appl. Phys. Lett.*, 2013, **102**, 033104.
- 276 Z. G. Fthenakis, Z. Zhu and D. Tomanek, *Phys. Rev. B: Condens. Matter Mater. Phys.*, 2014, **89**, 125421.
- 277 F. Long, P. Yasaei, R. Sanoj, W. Yao, P. Král, A. Salehi-Khojin and R. Shahbazian-Yassar, *ACS Appl. Mater. Interfaces*, 2016, **8**, 18360–18366.
- 278 R. M. d. Santos, L. E. d. Sousa, D. S. Galvão and L. A. Ribeiro, *Sci. Rep.*, 2020, **10**, 1–8.
- 279 L. Vicarelli, S. J. Heerema, C. Dekker and H. W. Zandbergen, *ACS Nano*, 2015, **9**, 3428–3435.
- 280 O. V. Yazyev and Y. P. Chen, *Nat. Nanotechnol.*, 2014, **9**, 755–767.
- 281 D. Wei, Y. Liu, Y. Wang, H. Zhang, L. Huang and G. Yu, *Nano Lett.*, 2009, **9**, 1752–1758.
- 282 X. Wang, X. Li, L. Zhang, Y. Yoon, P. K. Weber, H. Wang, J. Guo and H. Dai, *Science*, 2009, **324**, 768–771.
- 283 H. Wang, T. Maiyalagan and X. Wang, *ACS Catal.*, 2012, **2**, 781–794.
- 284 Y. Li, Z. Zhou, P. Shen and Z. Chen, *ACS Nano*, 2009, **3**, 1952–1958.
- 285 Y. Fujimoto and S. Saito, *Phys. Rev. B: Condens. Matter Mater. Phys.*, 2011, **84**, 245446.
- 286 P. Lambin, H. Amara, F. Ducastelle and L. Henrard, *Phys. Rev. B: Condens. Matter Mater. Phys.*, 2012, **86**, 045448.
- 287 N. Ansari, F. Nazari and F. Illas, *Phys. Chem. Chem. Phys.*, 2014, **16**, 21473–21485.
- 288 W. Brito, R. Kagimura and R. Miwa, *Phys. Rev. B: Condens. Matter Mater. Phys.*, 2012, **85**, 035404.
- 289 D. Berger and C. Ratsch, *Phys. Rev. B*, 2016, **93**, 235441.
- 290 Y. Liu, J. Song, Y. Li, Y. Liu and Q.-f. Sun, *Phys. Rev. B: Condens. Matter Mater. Phys.*, 2013, **87**, 195445.
- 291 D. Gunlycke and C. T. White, *Phys. Rev. Lett.*, 2011, **106**, 136806.
- 292 A. Rycerz, J. Tworzyczo and C. Beenakker, *Nat. Phys.*, 2007, **3**, 172–175.
- 293 A. Akhmerov and C. Beenakker, *Phys. Rev. Lett.*, 2007, **98**, 157003.
- 294 Y. Zhang, Z. Jiang, J. Small, M. Purewal, Y.-W. Tan, M. Fazlollahi, J. Chudow, J. Jaszczak, H. Stormer and P. Kim, *Phys. Rev. Lett.*, 2006, **96**, 136806.
- 295 Z. Zhu, A. Collaudin, B. Fauqué, W. Kang and K. Behnia, *Nat. Phys.*, 2012, **8**, 89–94.
- 296 W. Yao, D. Xiao and Q. Niu, *Phys. Rev. B: Condens. Matter Mater. Phys.*, 2008, **77**, 235406.
- 297 D. Gunlycke, S. Vasudevan and C. T. White, *Nano Lett.*, 2013, **13**, 259–263.



- 298 S. Haldar, R. G. Amorim, B. Sanyal, R. H. Scheicher and A. R. Rocha, *RSC Adv.*, 2016, **6**, 6702–6708.
- 299 O. V. Yazyev and S. G. Louie, *Phys. Rev. B: Condens. Matter Mater. Phys.*, 2010, **81**, 195420.
- 300 A. W. Tsen, L. Brown, M. P. Levendorf, F. Ghahari, P. Y. Huang, R. W. Havener, C. S. Ruiz-Vargas, D. A. Muller, P. Kim and J. Park, *Science*, 2012, **336**, 1143–1146.
- 301 C. Páez, A. Pereira, J. Rodrigues and N. Peres, *Phys. Rev. B: Condens. Matter Mater. Phys.*, 2015, **92**, 045426.
- 302 J. Sun, N. Lin, Z. Li, H. Ren, C. Tang and X. Zhao, *RSC Adv.*, 2016, **6**, 1090–1097.
- 303 F. Schedin, A. K. Geim, S. V. Morozov, E. W. Hill, P. Blake, M. I. Katsnelson and K. S. Novoselov, *Nat. Mater.*, 2007, **6**, 652–655.
- 304 H. E. Romero, P. Joshi, A. K. Gupta, H. R. Gutierrez, M. W. Cole, S. A. Tadigadapa and P. C. Eklund, *Nanotechnology*, 2009, **20**, 245501.
- 305 G. Ko, H.-Y. Kim, J. Ahn, Y.-M. Park, K.-Y. Lee and J. Kim, *Current Applied Physics*, 2010, **10**, 1002–1004.
- 306 C. Chen, S. Hung, M. Yang, C. Yeh, C. Wu, G. Chi, F. Ren and S. Pearton, *Appl. Phys. Lett.*, 2011, **99**, 243502.
- 307 H. J. Yoon, J. H. Yang, Z. Zhou, S. S. Yang and M. M.-C. Cheng, *Sens. Actuators, B*, 2011, **157**, 310–313.
- 308 G. T. Feliciano, C. Sanz-Navarro, M. D. Coutinho-Neto, P. Ordejón, R. H. Scheicher and A. R. Rocha, *Phys. Rev. Appl.*, 2015, **3**, 034003.
- 309 Y.-H. Zhang, Y.-B. Chen, K.-G. Zhou, C.-H. Liu, J. Zeng, H.-L. Zhang and Y. Peng, *Nanotechnology*, 2009, **20**, 185504.
- 310 Y.-H. Zhang, L.-F. Han, Y.-H. Xiao, D.-Z. Jia, Z.-H. Guo and F. Li, *Comput. Mater. Sci.*, 2013, **69**, 222–228.
- 311 A. R. Rocha, M. Rossi, A. Fazzio and A. J. da Silva, *Phys. Rev. Lett.*, 2008, **100**, 176803.
- 312 A. Rocha, M. Rossi, A. J. da Silva and A. Fazzio, *J. Phys. D: Appl. Phys.*, 2010, **43**, 374002.
- 313 R. G. Amorim, A. Fazzio, A. J. da Silva and A. R. Rocha, *Nanoscale*, 2013, **5**, 2798–2803.
- 314 B. Yang, H. Xu, J. Lu and K. P. Loh, *J. Am. Chem. Soc.*, 2014, **136**, 12041–12046.
- 315 K. Kim, Z. Lee, W. Regan, C. Kisielowski, M. Crommie and A. Zettl, *ACS Nano*, 2011, **5**, 2142–2146.
- 316 R. Grantab, V. B. Shenoy and R. S. Ruoff, *Science*, 2010, **330**, 946–948.
- 317 A. Ferreira, X. Xu, C.-L. Tan, S.-K. Bae, N. Peres, B.-H. Hong, B. Özyilmaz and A. C. Neto, *Europhys. Lett.*, 2011, **94**, 28003.
- 318 K. S. Novoselov, D. Jiang, F. Schedin, T. Booth, V. Khotkevich, S. Morozov and A. K. Geim, *Proc. Natl. Acad. Sci. U. S. A.*, 2005, **102**, 10451–10453.
- 319 A. C. Neto, F. Guinea, N. M. Peres, K. S. Novoselov and A. K. Geim, *Rev. Mod. Phys.*, 2009, **81**, 109.
- 320 N. M. Peres, *Rev. Mod. Phys.*, 2010, **82**, 2673.
- 321 D. Bahamon, A. Pereira and P. Schulz, *Phys. Rev. B: Condens. Matter Mater. Phys.*, 2011, **83**, 155436.
- 322 L. Jiang, X. Lv and Y. Zheng, *Phys. Lett. A*, 2011, **376**, 136–141.
- 323 Y. You, Z. Ni, T. Yu and Z. Shen, *Appl. Phys. Lett.*, 2008, **93**, 163112.
- 324 L. Brey and H. Fertig, *Phys. Rev. B: Condens. Matter Mater. Phys.*, 2006, **73**, 235411.
- 325 M. Ezawa, *Phys. Rev. B: Condens. Matter Mater. Phys.*, 2006, **73**, 045432.
- 326 M. Acik and Y. J. Chabal, *Jpn. J. Appl. Phys.*, 2011, **50**, 070101.
- 327 V. V. Ilyasov, B. Meshi, V. Nguyen, I. V. Ershov and D. Nguyen, *J. Appl. Phys.*, 2014, **115**, 053708.
- 328 Y. Li, Z. Zhou, C. R. Cabrera and Z. Chen, *Sci. Rep.*, 2013, **3**, 1–6.
- 329 C. Park, J. Ihm and G. Kim, *Phys. Rev. B: Condens. Matter Mater. Phys.*, 2013, **88**, 045403.
- 330 C. Park, H. Yang, A. J. Mayne, G. Dujardin, S. Seo, Y. Kuk, J. Ihm and G. Kim, *Proc. Natl. Acad. Sci. U. S. A.*, 2011, **108**, 18622–18625.
- 331 N. Marzari and D. Vanderbilt, *Phys. Rev. B: Condens. Matter Mater. Phys.*, 1997, **56**, 12847.
- 332 P. Koskinen, S. Malola and H. Häkkinen, *Phys. Rev. B: Condens. Matter Mater. Phys.*, 2009, **80**, 073401.
- 333 B. Huang, M. Liu, N. Su, J. Wu, W. Duan, B.-l. Gu and F. Liu, *Phys. Rev. Lett.*, 2009, **102**, 166404.
- 334 C. Reddy, A. Ramasubramaniam, V. Shenoy and Y.-W. Zhang, *Appl. Phys. Lett.*, 2009, **94**, 101904.
- 335 K. Nakada, M. Fujita, G. Dresselhaus and M. S. Dresselhaus, *Phys. Rev. B: Condens. Matter Mater. Phys.*, 1996, **54**, 17954.
- 336 T. Wassmann, A. P. Seitsonen, A. M. Saitta, M. Lazzeri and F. Mauri, *Phys. Rev. Lett.*, 2008, **101**, 096402.
- 337 L. Cancado, M. Pimenta, B. Neves, M. Dantas and A. Jorio, *Phys. Rev. Lett.*, 2004, **93**, 247401.
- 338 C. Casiraghi, A. Hartschuh, H. Qian, S. Piscanec, C. Georgi, A. Fasoli, K. Novoselov, D. Basko and A. Ferrari, *Nano Lett.*, 2009, **9**, 1433–1441.
- 339 Y. Niimi, T. Matsui, H. Kambara, K. Tagami, M. Tsukada and H. Fukuyama, *Phys. Rev. B: Condens. Matter Mater. Phys.*, 2006, **73**, 085421.
- 340 Z. Liu, K. Suenaga, P. J. Harris and S. Iijima, *Phys. Rev. Lett.*, 2009, **102**, 015501.
- 341 X. Jia, M. Hofmann, V. Meunier, B. G. Sumpter, J. Campos-Delgado, J. M. Romo-Herrera, H. Son, Y.-P. Hsieh, A. Reina and J. Kong, *Science*, 2009, **323**, 1701–1705.
- 342 M. Evaldsson, I. V. Zozoulenko, H. Xu and T. Heinzel, *Phys. Rev. B: Condens. Matter Mater. Phys.*, 2008, **78**, 161407.
- 343 J. Li, Z. Li, G. Zhou, Z. Liu, J. Wu, B.-L. Gu, J. Ihm and W. Duan, *Phys. Rev. B: Condens. Matter Mater. Phys.*, 2010, **82**, 115410.
- 344 T. Li and S.-P. Lu, *Phys. Rev. B: Condens. Matter Mater. Phys.*, 2008, **77**, 085408.
- 345 R. Golizadeh-Mojarad and S. Datta, *Phys. Rev. B: Condens. Matter Mater. Phys.*, 2007, **75**, 081301.
- 346 M. Buttiker, *IBM J. Res. Dev.*, 1988, **32**, 63–75.
- 347 G.-Y. Sun and Y.-j. Zhu, *J. Electron. Mater.*, 2013, **42**, 1–9.
- 348 L. Ju, B. Geng, J. Horng, C. Girit, M. Martin, Z. Hao, H. A. Bechtel, X. Liang, A. Zettl and Y. R. Shen, *Nat. Nanotechnol.*, 2011, **6**, 630–634.
- 349 D. Bischoff, J. Güttinger, S. Dröschner, T. Ihn, K. Ensslin and C. Stampfer, *J. Appl. Phys.*, 2011, **109**, 073710.



- 350 K. Brockdorf, Z. Ji, N. Engel, J. Myers, S. Mou, H. Huang and Y. Zhuang, *Mater. Lett.*, 2018, **211**, 183–186.
- 351 Z. Ji, J. Myers, K. Brockdorf, N. Engel, S. Mou, H. Huang and Y. Zhuang, *J. Vac. Sci. Technol.*, 2018, **36**, 05G508.
- 352 Z. Fei, A. Rodin, G. O. Andreev, W. Bao, A. McLeod, M. Wagner, L. Zhang, Z. Zhao, M. Thiemens and G. Dominguez, *Nature*, 2012, **487**, 82–85.
- 353 Z. Fei, M. Goldflam, J.-S. Wu, S. Dai, M. Wagner, A. McLeod, M. Liu, K. Post, S. Zhu and G. Janssen, *Nano Lett.*, 2015, **15**, 8271–8276.
- 354 V. W. Brar, M. S. Jang, M. Sherrott, J. J. Lopez and H. A. Atwater, *Nano Lett.*, 2013, **13**, 2541–2547.
- 355 K. Brenner, Y. Yang and R. Murali, *Carbon*, 2012, **50**, 637–645.
- 356 G. Ten, A. Y. Gerasimenko, M. S. Savelyev, A. V. Kuksin, P. N. Vasilevsky, E. P. Kitsyuk and V. I. Baranov, *Letters on Materials*, 2020, **10**, 89–93.
- 357 Z. Ni, W. Chen, X. Fan, J. Kuo, T. Yu, A. Wee and Z. Shen, *Phys. Rev. B: Condens. Matter Mater. Phys.*, 2008, **77**, 115416.
- 358 N. Mermin, *Phys. Rev. B: Condens. Matter Mater. Phys.*, 2006, **74**, 149902.
- 359 N. D. Mermin and H. Wagner, *Phys. Rev. Lett.*, 1966, **17**, 1133.
- 360 P. Xu, M. Neek-Amal, S. Barber, J. Schoelz, M. Ackerman, P. Thibado, A. Sadeghi and F. Peeters, *Nat. Commun.*, 2014, **5**, 1–7.
- 361 J. Venables, G. Spiller and M. Hanbucken, *Rep. Prog. Phys.*, 1984, **47**, 399.
- 362 M. Zinke-Allmang, L. C. Feldman and M. H. Grabow, *Surf. Sci. Rep.*, 1992, **16**, 377–463.
- 363 J. Evans, P. Thiel and M. C. Bartelt, *Surf. Sci. Rep.*, 2006, **61**, 1–128.
- 364 A. Fasolino, J. Los and M. I. Katsnelson, *Nat. Mater.*, 2007, **6**, 858–861.
- 365 F. Ding, H. Ji, Y. Chen, A. Herklotz, K. Dörr, Y. Mei, A. Rastelli and O. G. Schmidt, *Nano Lett.*, 2010, **10**, 3453–3458.
- 366 H. Pan and B. Chen, *Sci. Rep.*, 2014, **4**, 1–8.
- 367 V. M. Pereira, A. C. Neto and N. Peres, *Phys. Rev. B: Condens. Matter Mater. Phys.*, 2009, **80**, 045401.
- 368 H. Pan, *Mater. Chem. Phys.*, 2017, **189**, 111–117.
- 369 Q. Zhao, M. B. Nardelli and J. Bernholc, *Phys. Rev. B: Condens. Matter Mater. Phys.*, 2002, **65**, 144105.
- 370 P. Jensen, J. Gale and X. Blase, *Phys. Rev. B: Condens. Matter Mater. Phys.*, 2002, **66**, 193403.
- 371 Z. Li, P. Dharap, P. Sharma, S. Nagarajaiah and B. I. Yakobson, *J. Appl. Phys.*, 2005, **97**, 074303.
- 372 S. Deng and V. Berry, *Mater. Today*, 2016, **19**, 197–212.
- 373 N. Liu, Z. Pan, L. Fu, C. Zhang, B. Dai and Z. Liu, *Nano Res.*, 2011, **4**, 996–1004.
- 374 W. Zhu, T. Low, V. Perebeinos, A. A. Bol, Y. Zhu, H. Yan, J. Tersoff and P. Avouris, *Nano Lett.*, 2012, **12**, 3431–3436.
- 375 S. J. Chae, F. Güneş, K. K. Kim, E. S. Kim, G. H. Han, S. M. Kim, H. J. Shin, S. M. Yoon, J. Y. Choi and M. H. Park, *Adv. Mater.*, 2009, **21**, 2328–2333.
- 376 J. Zang, S. Ryu, N. Pugno, Q. Wang, Q. Tu, M. J. Buehler and X. Zhao, *Nat. Mater.*, 2013, **12**, 321–325.
- 377 X. Wang, K. Tantiwanichapan, J. W. Christopher, R. Paiella and A. K. Swan, *Nano Lett.*, 2015, **15**, 5969–5975.
- 378 A. L. Kitt, Z. Qi, S. Rémi, H. S. Park, A. K. Swan and B. B. Goldberg, *Nano Lett.*, 2013, **13**, 2605–2610.
- 379 L. Yang, Y. Guo and Q. Zhang, *Diamond Relat. Mater.*, 2017, **73**, 273–277.
- 380 Q. Bai, X. He, J. Bai and Z. Tong, *AIP Adv.*, 2016, **6**, 055308.
- 381 P. Yin and M. Ma, *ACS Appl. Nano Mater.*, 2018, **1**, 6596–6602.
- 382 X. Lin, H. Zhang, Z. Guo and T. Chang, *Tribol. Int.*, 2019, **131**, 686–693.
- 383 K. Wang, W. Ouyang, W. Cao, M. Ma and Q. Zheng, *Nanoscale*, 2019, **11**, 2186–2193.
- 384 Y. Dong, Z. Duan, Y. Tao, Z. Wei, B. Gueye, Y. Zhang and Y. Chen, *Tribol. Int.*, 2019, **136**, 259–266.
- 385 K. Wang, C. Qu, J. Wang, W. Ouyang, M. Ma and Q. Zheng, *ACS Appl. Mater. Interfaces*, 2019, **11**, 36169–36176.
- 386 Z. H. Ni, T. Yu, Y. H. Lu, Y. Y. Wang, Y. P. Feng and Z. X. Shen, *ACS Nano*, 2008, **2**, 2301–2305.
- 387 G. Gui, J. Li and J. Zhong, *Phys. Rev. B: Condens. Matter Mater. Phys.*, 2008, **78**, 075435.
- 388 M. Huang, T. A. Pascal, H. Kim, W. A. Goddard III and J. R. Greer, *Nano Lett.*, 2011, **11**, 1241–1246.
- 389 R. Ribeiro, V. M. Pereira, N. Peres, P. Briddon and A. C. Neto, *New J. Phys.*, 2009, **11**, 115002.
- 390 S.-M. Choi, S.-H. Jhi and Y.-W. Son, *Phys. Rev. B: Condens. Matter Mater. Phys.*, 2010, **81**, 081407.
- 391 Z. H. Ni, T. Yu, Y. H. Lu, Y. Y. Wang, Y. P. Feng, Z. X. Shen and T. Low, *ACS Nano*, 2009, **3**, 483.
- 392 M. Farjam and H. Rafii-Tabar, *Phys. Rev. B: Condens. Matter Mater. Phys.*, 2009, **80**, 167401.
- 393 S. Souma, Y. Ohmi and M. Ogawa, *J. Comput. Electron.*, 2013, **12**, 170–174.
- 394 Y. Wei and R. Yang, *Natl. Sci. Rev.*, 2019, **6**, 324–348.
- 395 D. G. Papageorgiou, I. A. Kinloch and R. J. Young, *Prog. Mater. Sci.*, 2017, **90**, 75–127.
- 396 Q. Cao, X. Geng, H. Wang, P. Wang, A. Liu, Y. Lan and Q. Peng, *Crystals*, 2018, **8**, 357.
- 397 E. Cadelano, P. L. Palla, S. Giordano and L. Colombo, *Phys. Rev. Lett.*, 2009, **102**, 235502.
- 398 C. Lee, X. Wei, J. W. Kysar and J. Hone, *Science*, 2008, **321**, 385–388.
- 399 F. Liu, P. Ming and J. Li, *Phys. Rev. B: Condens. Matter Mater. Phys.*, 2007, **76**, 064120.
- 400 I. Y. Sagalianov, T. M. Radchenko, Y. I. Prylutsky, V. A. Tatarenko and P. Szroeder, *Eur. Phys. J. B*, 2017, **90**, 1–9.
- 401 I. Y. Sahalianov, T. Radchenko, V. Tatarenko and Y. I. Prylutsky, *Ann. Phys.*, 2018, **398**, 80–93.
- 402 T. Radchenko, I. Sahalianov, V. Tatarenko, Y. Prylutsky, P. Szroeder, M. Kempniński and W. Kempniński, 2018, arXiv:1712.03424.
- 403 T. M. Radchenko, V. A. Tatarenko, V. V. Lizunov, V. B. Molodkin, I. E. Golentus, I. Y. Sahalianov and Y. I. Prylutsky, *Phys. Status Solidi B*, 2019, **256**, 1800406.
- 404 T. M. Radchenko, I. Y. Sahalianov, V. A. Tatarenko, Y. I. Prylutsky, P. Szroeder, M. Kempniński and



- W. Kempinski, *Handbook of Graphene Set*, 2019, vol. 1, pp. 451–502.
- 405 I. Y. Sahalianov, T. M. Radchenko, V. A. Tatarenko, G. Cuniberti and Y. I. Prylutskyy, *J. Appl. Phys.*, 2019, **126**, 054302.
- 406 A. Mehmood, N. Mubarak, M. Khalid, R. Walvekar, E. Abdullah, M. Siddiqui, H. A. Baloch, S. Nizamuddin and S. Mazari, *J. Environ. Chem. Eng.*, 2020, **8**, 103743.
- 407 X. Wang, H. Tian, W. Xie, Y. Shu, W.-T. Mi, M. Ali Mohammad, Q.-Y. Xie, Y. Yang, J.-B. Xu and T.-L. Ren, *NPG Asia Mater.*, 2015, **7**, e154.
- 408 F. Guinea, *Solid State Commun.*, 2012, **152**, 1437–1441.
- 409 C.-C. Hsu, M. Teague, J.-Q. Wang and N.-C. Yeh, *Sci. Adv.*, 2020, **6**, eaat9488.
- 410 S. Dai, Y. Xiang and D. J. Srolovitz, *Nano Lett.*, 2016, **16**, 5923–5927.
- 411 J. Hicks, M. Sprinkle, K. Shepperd, F. Wang, A. Tejada, A. Taleb-Ibrahimi, F. Bertran, P. Le Fèvre, W. De Heer and C. Berger, *Phys. Rev. B: Condens. Matter Mater. Phys.*, 2011, **83**, 205403.
- 412 E. S. Morell, P. Vargas, L. Chico and L. Brey, *Phys. Rev. B: Condens. Matter Mater. Phys.*, 2011, **84**, 195421.
- 413 G. Tarnopolsky, A. J. Kruchkov and A. Vishwanath, *Phys. Rev. Lett.*, 2019, **122**, 106405.
- 414 M. Anđelković, L. Covaci and F. Peeters, *Phys. Rev. Mater.*, 2018, **2**, 034004.
- 415 E. J. Mele, *Phys. Rev. B: Condens. Matter Mater. Phys.*, 2010, **81**, 161405.
- 416 B.-L. Huang, C.-P. Chuu and M.-F. Lin, *Sci. Rep.*, 2019, **9**, 1–12.
- 417 C.-Y. Lin, J.-Y. Wu, Y.-H. Chiu, C.-P. Chang and M.-F. Lin, *Phys. Rev. B: Condens. Matter Mater. Phys.*, 2014, **90**, 205434.
- 418 D. S. Lee, C. Riedl, T. Beringer, A. C. Neto, K. von Klitzing, U. Starke and J. H. Smet, *Phys. Rev. Lett.*, 2011, **107**, 216602.
- 419 C.-C. Lu, Y.-C. Lin, Z. Liu, C.-H. Yeh, K. Suenaga and P.-W. Chiu, *ACS Nano*, 2013, **7**, 2587–2594.
- 420 W. Yan, W.-Y. He, Z.-D. Chu, M. Liu, L. Meng, R.-F. Dou, Y. Zhang, Z. Liu, J.-C. Nie and L. He, *Nat. Commun.*, 2013, **4**, 1–7.
- 421 J. S. Alden, A. W. Tsen, P. Y. Huang, R. Hovden, L. Brown, J. Park, D. A. Muller and P. L. McEuen, *Proc. Natl. Acad. Sci. U. S. A.*, 2013, **110**, 11256–11260.
- 422 K. Kim, M. Yankowitz, B. Fallahazad, S. Kang, H. C. Movva, S. Huang, S. Larentis, C. M. Corbet, T. Taniguchi and K. Watanabe, *Nano Lett.*, 2016, **16**, 1989–1995.
- 423 L.-J. Yin, H. Jiang, J.-B. Qiao and L. He, *Nat. Commun.*, 2016, **7**, 1–6.
- 424 J. A. Garlow, L. K. Barrett, L. Wu, K. Kisslinger, Y. Zhu and J. F. Pulecio, *Sci. Rep.*, 2016, **6**, 1–11.
- 425 A. Vaezi, Y. Liang, D. H. Ngai, L. Yang and E.-A. Kim, *Phys. Rev. X*, 2013, **3**, 021018.
- 426 C. Woods, L. Britnell, A. Eckmann, R. Ma, J. Lu, H. Guo, X. Lin, G. Yu, Y. Cao and R. V. Gorbachev, *Nat. Phys.*, 2014, **10**, 451–456.
- 427 C. Gong, S. Lee, S. Hong, E. Yoon, G.-D. Lee and J. H. Warner, *Nanoscale*, 2017, **9**, 13725–13730.
- 428 M. W. Ochapski, D. Ataç, J. G. Sanderink, A. Y. Kovalgin and M. P. de Jong, *Carbon Trends*, 2021, **4**, 100045.
- 429 E. V. Castro, N. Peres and J. L. dos Santos, *Europhys. Lett.*, 2008, **84**, 17001.
- 430 S. Choi, B. W. Jeong, S. Kim and G. Kim, *J. Phys.: Condens. Matter*, 2008, **20**, 235220.
- 431 Y.-H. Kim, J. Choi, K.-J. Chang and D. Tománek, *Phys. Rev. B: Condens. Matter Mater. Phys.*, 2003, **68**, 125420.
- 432 J.-Y. Moon, M. Kim, S.-I. Kim, S. Xu, J.-H. Choi, D. Whang, K. Watanabe, T. Taniguchi, D. S. Park and J. Seo, *Sci. Adv.*, 2020, **6**, eabc6601.
- 433 P. Schweizer, C. Dolle and E. Spiecker, *Sci. Adv.*, 2018, **4**, eaat4712.
- 434 Q. Ye, J. Wang, Z. Liu, Z.-C. Deng, X.-T. Kong, F. Xing, X.-D. Chen, W.-Y. Zhou, C.-P. Zhang and J.-G. Tian, *Appl. Phys. Lett.*, 2013, **102**, 021912.
- 435 R. W. Havener, Y. Liang, L. Brown, L. Yang and J. Park, *Nano Lett.*, 2014, **14**, 3353–3357.
- 436 M. De Corato, C. Cocchi, D. Prezzi, M. J. Caldas, E. Molinari and A. Ruini, *J. Phys. Chem. C*, 2014, **118**, 23219–23225.
- 437 S. K. Jain, V. Juričić and G. T. Barkema, *2D Materials*, 2016, **4**, 015018.
- 438 S. Shallcross, S. Sharma and O. A. Pankratov, *Phys. Rev. Lett.*, 2008, **101**, 056803.
- 439 R. De Gail, M. Goerbig, F. Guinea, G. Montambaux and A. C. Neto, *Phys. Rev. B: Condens. Matter Mater. Phys.*, 2011, **84**, 045436.
- 440 R. Bistritzer and A. MacDonald, *Phys. Rev. B: Condens. Matter Mater. Phys.*, 2011, **84**, 035440.
- 441 G. Trambly de Laissardière, D. Mayou and L. Magaud, *Nano Lett.*, 2010, **10**, 804–808.
- 442 L. Meng, W. Yan, L. Yin, Z.-D. Chu, Y. Zhang, L. Feng, R. Dou and J. Nie, *J. Phys. Chem. C*, 2014, **118**, 6462–6466.
- 443 K. K. Saha, M. Drndić and B. K. Nikolic, *Nano Lett.*, 2012, **12**, 50–55.

